
This copy is for your personal, non-commercial use only.

If you wish to distribute this article to others, you can order high-quality copies for your colleagues, clients, or customers by [clicking here](#).

Permission to republish or repurpose articles or portions of articles can be obtained by following the guidelines [here](#).

The following resources related to this article are available online at www.sciencemag.org (this information is current as of March 4, 2011):

Updated information and services, including high-resolution figures, can be found in the online version of this article at:

<http://www.sciencemag.org/content/331/6021/1175.full.html>

Supporting Online Material can be found at:

<http://www.sciencemag.org/content/suppl/2011/03/01/331.6021.1175.DC1.html>

This article **cites 26 articles**, 9 of which can be accessed free:

<http://www.sciencemag.org/content/331/6021/1175.full.html#ref-list-1>

This article appears in the following **subject collections**:

Geochemistry, Geophysics

http://www.sciencemag.org/cgi/collection/geochem_phys

Planetary Science

http://www.sciencemag.org/cgi/collection/planet_sci

(58/42) proportions corresponding to a slight bias in favor of one station. Upon titrating **1** with an acid, the smaller NMR signals disappear without any measurable delay during the measurement of a ^1H NMR spectrum (~ 2 min), and only one set of signals remains after adding excess acid (Fig. 3, D and E). This is consistent with the trapping of **1** on a single station of **9**, as it is repelled by the ammonium function of the other station. Adding a base instantly reverses the process. Again, the time scale of this controlled motion is much faster than the rates of unfolding and refolding of **1** around **9**, implying that motion is mediated by the rapid sliding of **1** along **9**.

Using helices longer than **1** should expectedly result in slower sliding but also in much slower helix-rod dissociation. Combining rods with multiple distinct stations with mixtures of helices of different lengths should thus allow several controlled motions to proceed at different rates within a single supramolecular construct.

References and Notes

- W. R. Browne, B. L. Feringa, *Nat. Nanotechnol.* **1**, 25 (2006).
- C. Mao, W. Sun, Z. Shen, N. C. Seeman, *Nature* **397**, 144 (1999).
- T. R. Kelly, H. De Silva, R. A. Silva, *Nature* **401**, 150 (1999).
- S. P. Fletcher, F. Dumur, M. M. Pollard, B. L. Feringa, *Science* **310**, 80 (2005).
- M. Muraoka, K. Kinbara, T. Aida, *Nature* **440**, 512 (2006).
- K. Miwa, Y. Furusho, E. Yashima, *Nat. Chem.* **2**, 444 (2010).
- S. Hiraoka, E. Okuno, T. Tanaka, M. Shiro, M. Shionoya, *J. Am. Chem. Soc.* **130**, 9089 (2008).
- J. D. Badjic, V. Balzani, A. Credi, S. Silvi, J. F. Stoddart, *Science* **303**, 1845 (2004).
- J. E. Green *et al.*, *Nature* **445**, 414 (2007).
- V. Serreli, C.-F. Lee, E. R. Kay, D. A. Leigh, *Nature* **445**, 523 (2007).
- M. R. Panman *et al.*, *Science* **328**, 1255 (2010).
- P. Mobian, J.-M. Kern, J.-P. Sauvage, *Angew. Chem. Int. Ed.* **43**, 2392 (2004).
- K. Kinbara, T. Aida, *Chem. Rev.* **105**, 1377 (2005).
- I. Huc, *Eur. J. Org. Chem.* **2004**, 17 (2004).
- V. Berl, I. Huc, R. G. Khoury, M. J. Krische, J.-M. Lehn, *Nature* **407**, 720 (2000).
- Materials and methods are detailed in supporting material at Science Online.
- E. Berni *et al.*, *Chem. Commun. (Camb.)* **2008** (no. 17), 1968 (2008).
- C. Bao *et al.*, *Angew. Chem. Int. Ed.* **47**, 4153 (2008).
- N. Delsuc *et al.*, *ChemPhysChem* **9**, 1882 (2008).
- B. Baptiste *et al.*, *Chem. Asian J.* **5**, 1364 (2010).
- Y. Cohen, L. Avram, L. Frish, *Angew. Chem. Int. Ed.* **44**, 520 (2005).
- T. Nishinaga, A. Tanatani, K. Oh, J. S. Moore, *J. Am. Chem. Soc.* **124**, 5934 (2002).
- A. Tanatani, T. S. Hughes, J. S. Moore, *Angew. Chem. Int. Ed.* **41**, 325 (2002).
- A. Petitjean, L. A. Cuccia, M. Schmutz, J.-M. Lehn, *J. Org. Chem.* **73**, 2481 (2008).
- C. A. Hunter *et al.*, *Angew. Chem. Int. Ed.* **40**, 2678 (2001).
- S.-Y. Chang, H.-Y. Jang, K.-S. Jeong, *Chemistry* **9**, 1535 (2003).
- P. T. Glink, A. I. Oliva, J. Stoddart, A. J. P. White, D. J. Williams, *Angew. Chem. Int. Ed.* **40**, 1870 (2001).
- M. Horn, J. Ihringer, P. T. Glink, J. F. Stoddart, *Chemistry* **9**, 4046 (2003).
- C. L. Perrin, T. J. Dwyer, *Chem. Rev.* **90**, 935 (1990).
- This work was supported by the CNRS, the Conseil Régional d'Aquitaine, the Chinese Academy of Sciences, and the National Natural Science Foundation of China (20772127, 20972164). We thank C. Müller-Dieckmann for beamtime and help during data collection on ID29 at the European Synchrotron Radiation Facility. Crystallographic data for (**3**)₂, (**2**)₂, **2**•**6**, **1**•**7**, **1**•**5**, and **1**•**8** have been deposited with the Cambridge Crystallographic Data Centre under reference numbers CCDC-797906, 797911, 797907, 797908, 797910, and 797909, respectively.

Supporting Online Material

www.sciencemag.org/cgi/content/full/331/6021/1172/DC1
Materials and Methods
Figs. S1 to S31
Tables S1 to S9
References

8 November 2010; accepted 20 January 2011
10.1126/science.1200143

Oxygen Isotope Variations at the Margin of a CAI Records Circulation Within the Solar Nebula

Justin I. Simon,^{1,2*} Ian D. Hutcheon,³ Steven B. Simon,⁴ Jennifer E. P. Matzel,³ Erick C. Ramon,³ Peter K. Weber,³ Lawrence Grossman,⁴ Donald J. DePaolo²

Micrometer-scale analyses of a calcium-, aluminum-rich inclusion (CAI) and the characteristic mineral bands mantling the CAI reveal that the outer parts of this primitive object have a large range of oxygen isotope compositions. The variations are systematic; the relative abundance of ^{16}O first decreases toward the CAI margin, approaching a planetary-like isotopic composition, then shifts to extremely ^{16}O -rich compositions through the surrounding rim. The variability implies that CAIs probably formed from several oxygen reservoirs. The observations support early and short-lived fluctuations of the environment in which CAIs formed, either because of transport of the CAIs themselves to distinct regions of the solar nebula or because of varying gas composition near the proto-Sun.

Calcium-, aluminum-rich inclusions (CAIs) are understood to have formed very early in the evolution of the solar system and in contact with nebular gas, either as solid condensates or as molten droplets. In general, CAIs are ^{16}O -rich relative to planetary materials and are believed to record the $\Delta^{17}\text{O}$ (I) composition of solar nebular gas in which they grew (2). $\Delta^{17}\text{O}$ may be a marker of radial position within the solar nebula. Less prim-

itive nebular materials (such as iron-, magnesium-rich chondrules) typically have planetary-like values ($\Delta^{17}\text{O} = 0$) and may have formed further out in the protoplanetary disk from where CAIs formed (3). Previous oxygen isotopic studies document substantial variation in the $\Delta^{17}\text{O}$ of CAIs (2, 4), but because of their lower spatial resolution ($\geq 10\ \mu\text{m}$) have not been able to probe the isotopic stratigraphy of the outer parts of CAIs with enough resolution to detect the continuous range of isotopic variations observed here. Because models suggest that radial transport of primitive matter may have played an important role in the evolution of protoplanetary disks (5–7), evidence within individual CAIs for transfer among distinct regions in the solar nebula, such as systematic $\Delta^{17}\text{O}$ variations, is of critical importance.

To further investigate intra-CAI oxygen isotopic variations, a component of the CV3 carbonaceous chondrite Allende (the CAI called A37), its surrounding concentric rim, and a micro-CAI enclosed within this rim were measured with NanoSIMS, an ion microprobe with nanometer-scale spatial resolution. Measurements were obtained as $\sim 2\text{-}\mu\text{m}$ spot analyses spaced every 7 to 10 μm across the rim and the outer $\sim 150\ \mu\text{m}$ of the interior (Fig. 1) (8). At the resolution that is accessible with NanoSIMS, both A37 and its rim exhibit more than 20 per mil (‰) variation in $\Delta^{17}\text{O}$, a range that is close to the full range thought to exist among solids formed in the solar system. Mass-dependent physicochemical processes cannot produce variations in $\Delta^{17}\text{O}$. These data imply that A37 was transported among several different nebular oxygen isotopic reservoirs (4), potentially as it passed through and/or into various regions of the protoplanetary disk.

Concentric multi-mineralic rim sequences [so-called Wark-Lovering (WL) rims (9)] are a widespread feature that indicates that many CAIs shared a similar evolution history to each other and possibly to less primitive materials, despite the compositional and mineralogical diversity of their interiors. These ubiquitous WL rims formed late—although still relatively early in solar system history according to evidence that they initially contained a canonical abundance of the short-lived nuclide ^{26}Al (10). The preservation of their primitive age attests to the fact that they have experienced minimal subsequent disturbance either in the nebula or on the chondrite parent body. The mineralogy and composition of the WL rims surrounding CAIs suggest that late in their evolution, the CAIs were in a nebular environment distinct from that where they origi-

¹Astromaterials Research Office KR111, NASA Johnson Space Center, Houston, TX 77058, USA. ²Center for Isotope Geochemistry, University of California, Berkeley, Berkeley, CA 94720, USA. ³Lawrence Livermore National Laboratory (LLNL), Livermore, CA 94551, USA. ⁴Department of Geophysical Sciences, University of Chicago, Chicago, IL 60637, USA.

*To whom correspondence should be addressed. E-mail: justin.i.simon@nasa.gov

nated and closer in composition to the environment in which the building materials of the terrestrial planets formed (10).

The CAI studied here (A37) is a ~7- by 4-mm compact Type A inclusion. A37 is composed primarily of the minerals melilite [Ak_{20-40} (11)], 20- to 70- μm -sized spinel, anhedral perovskite and rare fassaite that mainly occurs between the melilite grains (Fig. 1) (12). The surrounding WL rim is ~50 to 100 μm thick and is made up of a typical layered mineral sequence. Both the interior and WL rim data exhibit large variations in $\Delta^{17}\text{O}$ (Figs. 2 and 3). Heterogeneity in $\Delta^{17}\text{O}$ has been explained by isotopic mixing between an ^{16}O -rich reservoir composed of refractory materials and a second reservoir (probably nebular gas) with a more “planetary-like” isotopic composition (13). On an oxygen three-isotope plot, the data for A37 scatter about and along the carbonaceous chondrite anhydrous mineral (CCAM) line (Fig. 2). Linear regression of the CAI interior data and WL rim data yields slopes of 0.89 ± 0.06 (2 σ) and 0.96 ± 0.05 (2 σ), respectively. A majority of the spinel \pm hibonite spots in the WL rim have $\Delta^{17}\text{O}$ values less than -20‰ , which is comparable with spinel in the interior of other Allende CAIs (14) and equal to or lower than the melilite in the interior of A37, spinel in the micro-CAI, and the composition of many other unequilibrated inclusions (3).

The oxygen isotope zoning, from ^{16}O -rich values ($\Delta^{17}\text{O} \approx -20\text{‰}$) in the interior to near planetary-like values ($=0\text{‰}$) at the edge (Fig. 3), cannot be explained by igneous processes and is mostly likely secondary in origin. The inferred pre-rim history therefore involves the CAI first solidifying with a uniform enrichment of ^{16}O and then partially exchanging its oxygen with a second reservoir, most likely a nebular gas of planetary isotopic composition (15, 16). The detailed melilite oxygen-zoning profiles (Fig. 3) (8) provide support for this model in that they exhibit the same range of $\Delta^{17}\text{O}$ and nearly identical $\Delta^{17}\text{O}$ boundary-layer thicknesses.

We modeled solid-gas exchange of oxygen isotopes in A37 to investigate the possibility that the $\Delta^{17}\text{O}$ isotope profiles developed after crystallization and after the CAI was transferred from its place of origin to a distinct gaseous nebular reservoir (Fig. 4). For this, we obtained numerical solutions to the time-dependent diffusion equation in radial coordinates. Oxygen was assumed to diffuse within the solid in response to a change in the isotopic composition of oxygen in surrounding gas. The equation used is

$$\frac{\partial C_{i,\text{cond}}}{\partial t} = D_i \left(\frac{\partial C_{i,\text{cond}}}{\partial r^2} + \frac{2}{r} \frac{\partial C_{i,\text{cond}}}{\partial r} \right) \quad (1)$$

where $C_{i,\text{cond}}$ is the concentration of species i in the inclusion, D_i is the diffusivity of the isotope of interest in the inclusion (16), r is the radius of the inclusion, and t is time. The zoning in the model comes from solving the diffusion equation subject to constant concentrations of ^{16}O , ^{17}O ,

and ^{18}O at the gas-solid interface and assigning a uniform low- $\Delta^{17}\text{O}$ initial value to the CAI interior. The boundary condition at the CAI surface corresponds to a constant partial pressure of oxygen with a fixed (planetary-like) $\Delta^{17}\text{O}$ isotopic composition. The planetary $\Delta^{17}\text{O}$ value of the low-sodium melilite at the interface with hibonite/spinel, which is believed to be related to growth of the WL rims (fig. S2), is used to define the near-zero $\Delta^{17}\text{O}$ value at the hypothesized gas-CAI boundary. The $\Delta^{17}\text{O}$ value common to the CAI interior is used to estimate the enriched abundance of ^{16}O of the CAI before exchange with gas. The oxygen concentration of the gas is

based on a solar bulk composition at 10^{-3} bar total pressure (17, 18), and the concentration of oxygen in melilite is estimated by stoichiometry from electron probe analyses (8).

The systematic ^{16}O depletion in the outer margin of A37 can be fit with solid-state diffusional relaxation after an instantaneous change in the isotopic composition of the gas surrounding the CAIs (Fig. 4). Oxygen isotope exchange through self-diffusion is inferred to be the dominant mechanism in the development of the isotopic zoning profiles; the process is one involving only exchange of oxygen atoms between the CAI and the gas, with no other coupled chemical diffu-

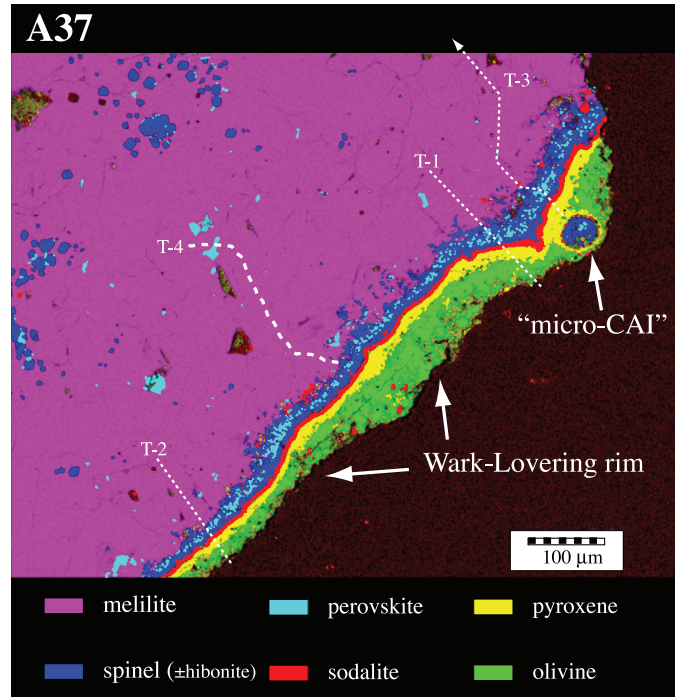


Fig. 1. Compositional x-ray image of the rim and margin of A37, a typical Type A CAI within the Allende meteorite. Oxygen isotope data were measured along traverses 1, 2, and 3 (by NanoSIMS), and compositional data were obtained from traverse 4 (by electron microprobe).

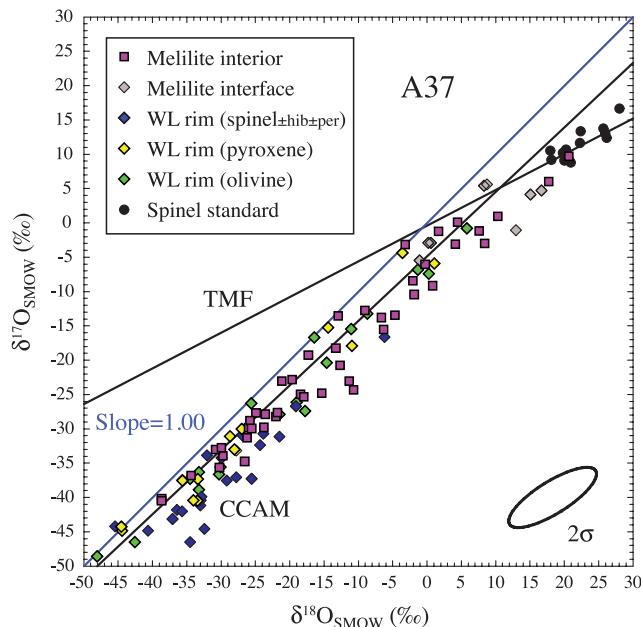


Fig. 2. Oxygen isotopic composition of refractory inclusion (A37) and rim. Data fall along the slope ~0.94 CCAM line. Terrestrial mass fractionation (TMF) line (slope = 0.52) and primordial mixing line (slope = 1.00) are shown for reference. Error ellipse represents 2 σ external reproducibility of measurements.

sion. The time necessary to develop the radial ^{16}O depletions represented by traverses 1, 2, and 3 depends on the assumed temperature because of

the strong dependence of D_0 on temperature. The time scale is ~ 150 years at temperatures near the liquidus (~ 1700 K), but much longer ($\sim 530,000$

Fig. 3. Oxygen isotope zoning across the WL rim and outer margin typical of A37, defined by ion microprobe traverses. Black and white scale bars, $10\ \mu\text{m}$ per increment. Horizontal band $\Delta^{17}\text{O} = -15$ to -20 is representative of interior. Colors correspond to different phases as in Fig. 1.

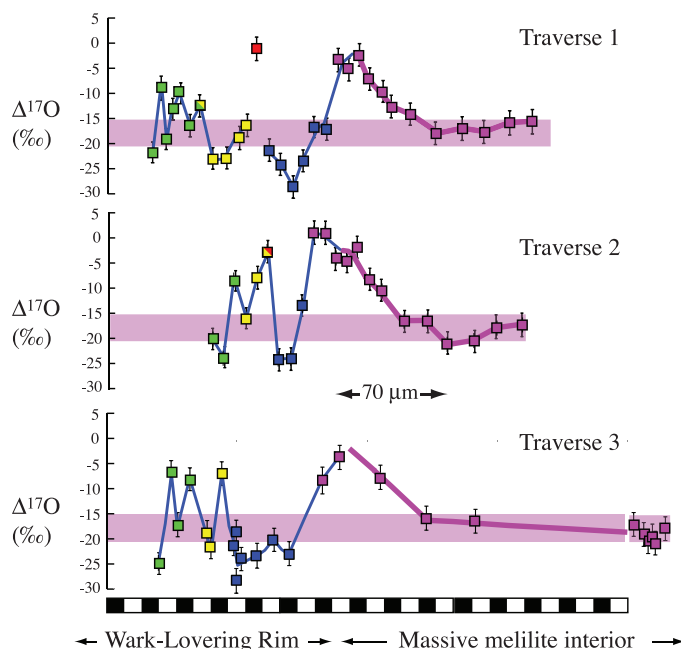
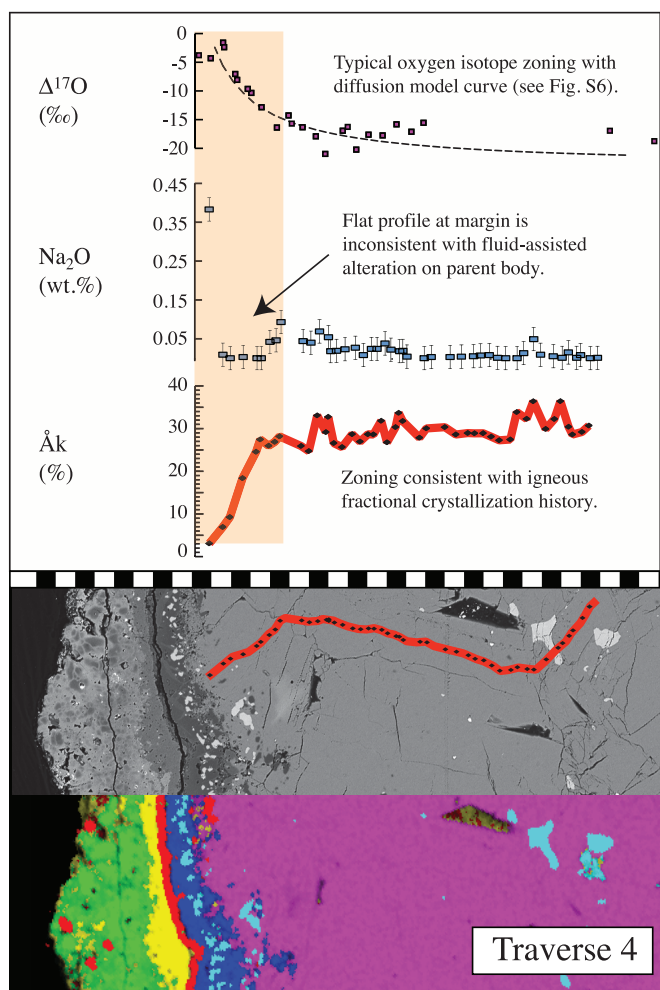


Fig. 4. Oxygen self-diffusion model compared with the isotope zoning of A37. Electron microprobe data show representative compositional [Åk (11) and sodium] zoning profiles (traverse 4) across the outer margin of melilite. Typical errors are shown for Na_2O . Black and white scale bars, $10\ \mu\text{m}$ per increment. Backscattered electron imaging (gray scale) and x-ray mapping (mineral color-coding as in other figures) accompany the electron probe data.



years) at $1200\ \text{K}$. Calculations (16) place an upper limit of $1600\ \text{K}$ (and thus a lower limit of ~ 500 years) for the integrated reaction period of diffusive exchange on the basis of the fact that spinels within the interior of CAIs are commonly ^{16}O -rich (have exchanged $<5\%$ of their original ^{16}O -excesses) despite their small size ($\sim 50\ \mu\text{m}$). Isotopic exchange could have occurred by reheating in numerous short (hours to days) events (19)—for example, as the result of time (10^2 to 10^3 years) within ^{16}O -poor gas subjected to shockwaves (20), which is similar to the environment envisioned for chondrule formation (21, 22). Temperatures of $\leq 1000\ \text{K}$, the maximum obtained within undifferentiated planetesimals, require unreasonable heating times (>100 million years) to fit the data, given both the thermal histories of chondrite parent bodies (23) and the primitive age of the surrounding WL rims (10). The flat sodium profile across the outer margin of the melilite interior (Fig. 4) is inconsistent with transport of sodium inward after the rim formed. Thus, there is no evidence that the oxygen isotope profiles are related to fluid-assisted alteration processes on the chondrite parent body (14).

A simple model in which CAI minerals exchange with a planetary-like oxygen reservoir (15, 16) would suffice if the WL rims had uniform oxygen isotopic compositions similar to that of the CAI margin—that is, close to the terrestrial planets. This scenario is complicated by the ^{16}O -enriched composition of most of the WL rim mineral bands. Because the WL rim data scatter nearly continuously along the CCAM line, as the rim grew A37 probably experienced isotopic exchange with a planetary-like gas reservoir that was not on the primordial slope = 1.00 mixing line. Detailed textural and mineralogical investigations at the CAI-rim interface reveal a ~ 1 - to $5\text{-}\mu\text{m}$ -thick, discontinuous zone of melilite between the gehlenitic interior and the spinel \pm hibonite of the rim that is åkermanite -rich and relatively sodium-poor (fig. S2). This relatively ^{16}O -poor zone may reflect new growth of magnesium-rich melilite or metamorphism of existing melilite that occurred concurrently with oxygen exchange and seems to mark a transition between growth from ^{16}O -rich to growth from ^{16}O -poor gas. This melilite possibly reflects the beginning of WL rim formation and implies that, initially, the rim grew from a ^{16}O -poor, planetary-like reservoir.

The transition from the åkermanite -rich melilite layer to the spinel \pm hibonite layer (a distance of no more than $10\ \mu\text{m}$) records the change in oxygen isotope composition from planetary-like back to the most ^{16}O -enriched reservoir recognized in the solar system. Conceivably, the CAI and WL rim could have formed from a ^{16}O -rich gas followed by immersion in a ^{16}O -poor one. However, the large variability in $\Delta^{17}\text{O}$, specifically the inward-increasing trends within spinel (and other rim minerals), implies that late-stage mineral-specific, diffusion-driven oxygen isotope exchange with a single external reservoir is unlikely to explain the rim record (4). The pyroxene and olivine rim data within each traverse show

some individual and some shared zoning behavior (for example, early pyroxene appears to have grown from a more planetary-like gas) but in general imply growth from relatively ^{16}O -rich gas. Varying isotopic composition in the pyroxene layer is consistent with the range of $\text{Ti}^{3+}/\text{Ti}^{4+}$ ratios reported for rim pyroxene (10, 24), possibly reflecting formation in more ^{16}O -poor (likely oxidizing) and ^{16}O -rich (likely reducing) environments (10). Given the large variations in $\Delta^{17}\text{O}$ that exist within the WL rim and the outer margin of the melilite interior of A37, the data require exposure of the inclusion to several (at least two) distinct nebular oxygen reservoirs in addition to the one from which it formed. We believe that the inclusion condensed from an ^{16}O -rich gas and was subsequently exposed to ^{16}O -poor and then ^{16}O -rich reservoirs. Collectively, this isotopic and petrologic record provides our best account of the transfer of CAIs among distinct nebular settings within the protoplanetary disk.

Young protoplanetary disks evolve through viscous accretion to the star coupled with outward transport of angular momentum. The evidence reported here supports expectations that radial transport of solid matter—perhaps in both directions—is a basic consequence of protoplanetary disk evolution (5, 25, 26). Large-scale radial circulation of nebular solids is also consistent with the reports of crystalline material located in the outer reaches of our solar system (27, 28) and in the outer, cool regions of distant stars (29, 30). The variable but largely ^{16}O -rich

composition of the WL rim suggests that after transport out of the inner solar system, CAIs either continued to form within a region in the outer solar system that varied in composition or that they were returned back to the inner solar system. Whether CAIs shared any common history with other nebular materials, such as early forming chondrules, is uncertain.

References and Notes

- $\Delta^{17}\text{O}$ reflects the deviation of the oxygen isotopic composition from the terrestrial fractionation line, where $\Delta^{17}\text{O} = \delta^{17}\text{O} - 0.528\delta^{18}\text{O}$. $\delta^{17}\text{O}$ and $\delta^{18}\text{O}$ reflect the per mil difference from the composition of standard mean ocean water (SMOW) so that $\delta^i\text{O}_{\text{SMOW}} = 10^3[(\text{O}^{16}\text{O})/(\text{O}^{16}\text{O})_{\text{SMOW}} - 1]$ and where i refers to either 17 or 18.
- R. N. Clayton, N. Onuma, L. Grossman, T. K. Mayeda, *Earth Planet. Sci. Lett.* **34**, 209 (1977).
- K. D. McKeegan, L. A. Leshin, S. S. Russell, G. J. MacPherson, *Science* **280**, 414 (1998).
- A. N. Krot, K. D. McKeegan, L. A. Leshin, G. J. MacPherson, E. R. D. Scott, *Science* **295**, 1051 (2002).
- F. H. Shu, H. Shang, T. Lee, *Science* **271**, 1545 (1996).
- J. N. Cuzzi, R. C. Hogan, K. Shariff, *Astrophys. J.* **687**, 1432 (2008).
- F. Ciesla, *Icarus* **200**, 655 (2009).
- Materials and methods are available as supporting material on Science Online.
- D. A. Wark, J. F. Lovering, *Proc. Lunar Sci. Conf.* **8**, 95 (1977).
- J. I. Simon *et al.*, *Earth Planet. Sci. Lett.* **238**, 272 (2005).
- The mineral melilite exhibits a compositional range between åkermanite [$\text{Ca}_2(\text{MgSi}_2\text{O}_7)$] and gehlenite [$\text{Ca}_2(\text{Al}_2\text{SiO}_7)$] end members, where $\text{Åk} = \text{Mg cation (\%)}$.
- S. B. Simon, A. M. Davis, L. Grossman, *Geochim. Cosmochim. Acta* **63**, 1233 (1999).
- R. N. Clayton, L. Grossman, T. K. Mayeda, *Science* **182**, 485 (1973).
- A. N. Krot *et al.*, *Geochim. Cosmochim. Acta* **72**, 2534 (2008).
- G. J. MacPherson, L. Grossman, *Earth Planet. Sci. Lett.* **52**, 16 (1981).
- F. J. Ryerson, K. D. McKeegan, *Geochim. Cosmochim. Acta* **58**, 3713 (1994).
- L. Grossman *et al.*, *Geochim. Cosmochim. Acta* **64**, 2879 (2000).
- C. M. O. Alexander, *Geochim. Cosmochim. Acta* **68**, 3943 (2004).
- E. D. Young *et al.*, *Science* **308**, 223 (2005).
- J. A. Wood, *Meteorit. Planet. Sci.* **31**, 641 (1996).
- H. C. Connolly Jr., S. G. Love, *Science* **280**, 62 (1998).
- L. L. Hood, M. Horanyi, *Icarus* **106**, 179 (1993).
- E. D. Young, *Philos. Trans. R. Soc. London A* **359**, 2095 (2001).
- S. B. Simon, S. R. Sutton, L. Grossman, *Geochim. Cosmochim. Acta* **71**, 3098 (2007).
- J. N. Cuzzi, S. S. Davis, A. R. Dobrovolskis, *Icarus* **166**, 385 (2003).
- F. J. Ciesla, *Science* **318**, 613 (2007).
- J. Crovisier *et al.*, *Science* **275**, 1904 (1997).
- D. Brownlee *et al.*, *Science* **314**, 1711 (2006).
- R. van Boekel *et al.*, *Nature* **432**, 479 (2004).
- D. Apai *et al.*, *Science* **310**, 834 (2005).
- This work was supported by grants from the Institute of Geophysics and Planetary Physics at LLNL (J.I.S. and D.J.D.), the NASA Origins program (I.D.H., J.E.P.M., and J.I.S.), and the NASA Cosmochemistry program (L.G. and I.D.H.). Work was performed under the auspices of the U.S. Department of Energy at LLNL under contract DE-AC52-07NA27344.

Supporting Online Material

www.sciencemag.org/cgi/content/full/331/6021/1175/DC1
Materials and Methods
Figs. S1 to S5
Tables S1 to S3
References

20 September 2010; accepted 26 January 2011
10.1126/science.1197970

Dietary Change and Evolution of Horses in North America

Matthew C. Mhlbachler,^{1,2*} Florent Rivals,³ Nikos Solounias,^{1,2} Gina M. Semperebon⁴

The evolution of high-crowned molars among horses (Family Equidae) is thought to be an adaptation for abrasive diets associated with the spread of grasslands. The sharpness and relief of the worn cusp apices of teeth (mesowear) are a measure of dietary abrasion. We collected mesowear data for North American Equidae for the past 55.5 million years to test the association of molar height and dietary abrasion. Mesowear trends in horses are reflective of global cooling and associated vegetation changes. There is a strong correlation between mesowear and crown height in horses; however, most horse paleopopulations had highly variable amounts of dietary abrasion, suggesting that selective pressures for crown height may have been weak much of the time. However, instances of higher abrasion were observed in some paleopopulations, suggesting intervals of stronger selection for the evolution of dentitions, including the early Miocene shortly before the first appearance of Equinae, the horse subfamily in which high-crowned dentitions evolved.

The evolution of high-crowned molars (hypsodonty) in horses and other mammalian herbivores is a classic hypothesis of adaptation (1–3), thought to have evolved as a response to increased dental wear associated with changes in habitat structure that caused a higher degree of dietary abrasion, such as the spread of phytolith-bearing grasslands and the increased consumption of dust in increasingly arid environments (4–10). The earliest horses

from ~55.5 million years ago (Ma) had short-crowned (brachydont) molars with poorly developed shearing crests, suggesting a frugivorous diet. During the Eocene and Oligocene, horses acquired shearing lophs on their molars, suggesting a shift toward leafy browsing. The subfamily Equinae, which includes living horses, appeared in the early Miocene (~18 Ma). These horses show increased crown height, increased occlusal surface complexity, and thickened cementum. The appear-

ance of Equinae suggests a shift toward grazing (grass-eating) diets; however, paleosols and fossil phytolith assemblages suggest that grassy habitats were present in the North American Great Plains millions of years earlier (11–14). The earliest Equinae had intermediate crown heights (mesodont), whereas high-crowned (hypsodont) horses appeared millions of years later. Explanations for the delayed evolution of hypsodonty are that selection was weak or episodic, or that phylogenetic constraints caused horses to resist feeding in open grasslands for several million years (13).

To further understand the coevolution of horses and their paleodiets, we examined mesowear patterns in the molars of North American fossil horses from their first appearance (~55.5 Ma) to their extinction in North America (~0.01 Ma) (15). Their geographic coverage includes nearly all of the fossiliferous regions of North America; the greatest concentration of data is from the Great Plains. Mesowear is a macroscopic dietary

¹Department of Anatomy, New York College of Osteopathic Medicine, Old Westbury, NY 11568, USA. ²Division of Paleontology, American Museum of Natural History, New York, NY 10024, USA. ³ICREA, Institut Català de Paleoecologia Humana i Evolució Social, Universitat Rovira i Virgili, 43002 Tarragona, Spain. ⁴Department of Biology, Bay Path College, Longmeadow, MA 01106, USA.

*To whom correspondence should be addressed. E-mail: mmhlbac@nyit.edu



www.sciencemag.org/cgi/content/full/331/6021/1175/DC1

Supporting Online Material for

**Oxygen Isotope Variations at the Margin of a CAI Records Circulation
Within the Solar Nebula**

Justin I. Simon,* Ian D. Hutcheon, Steven B. Simon, Jennifer E. P. Matzel,
Erick C. Ramon, Peter K. Weber, Lawrence Grossman, Donald J. DePaolo

*To who correspondence should be addressed. E-mail: justin.i.simon@nasa.gov

Published 4 March 2011, *Science* **331**, 1175 (2010)
DOI: 10.1126/science.1197790

This PDF file includes:

Materials and Methods

Figs. S1 to S5

Tables S1 to S3

References

Science Online Methods and Materials:

Analytical Methods: The inclusion A37 and its WL rim were analyzed by ion and electron microprobes and scanning electron microscopes. Oxygen isotopic variation in the CAI and surrounding rim was measured with the NanoSIMS, a secondary ion microprobe with nanometer-scale spatial resolution at Lawrence Livermore National Laboratory (LLNL) (Table S1). Measurements were performed by sputtering a polished, carbon-coated thick section with a 16 keV, ~12 pA Cs⁺ beam focused to produce a spot size of about 1.5x2.0 µm at the sample surface. Although still very small, the beam size used was larger than most NanoSIMS work in order to improve ion sensitivity, and thus the counting statistics. Negative secondary ions of ¹⁶O, ¹⁷O, ¹⁸O, and ²⁹Si were collected in a Faraday cup and three electron multiplier (EM) detectors, respectively, in isotope ratio mode. Each measurement had between 300,000 and 600,000 counts of ¹⁷O and 1,500,000 and 3,000,000 counts of ¹⁸O collected during 500 one-second cycles, for a total analysis time of 500 seconds. The reported uncertainties based on these count rates follow a Poisson distribution as is expected. A mass resolving power of ~7000 was used to sufficiently separate ¹⁷O from ¹⁶OH. The ²⁹Si/¹⁶O ratio allowed us to identify which minerals were analyzed (in addition to pre- and post- analysis BSE and x-ray imagery), which was critical for interpreting the WL rim data. A normal-incidence electron gun was utilized for charge compensation. We evaluated instrumental mass fractionation (IMF) and our analytical reproducibility by repeat analyses of terrestrial spinel and anorthite standards. The good agreement of the measured values to their known reference values (e.g., (1) and S. Krot, personal communication, respectively) indicates that under our analytical conditions, IMF is small and linear (i.e., significant mineral specific matrix effects can be avoided). In particular, as described below in more detail the method introduces negligible mass *independent* effects between the analyzed oxide and silicate minerals. Although few similar NanoSIMS studies exist, cf. (2), conventional SIMS oxygen isotope studies typically evaluate potential matrix effects by similar means. In general, matrix effects are anticipated to be relatively small because mainly minerals with similar (i.e., relatively low) FeO contents relative to the spinel standard were measured, cf. (3). Furthermore, because matrix effects cause only a shift in IMF, and since potential departures from a linear mass fractionation law are negligible for the few per mil/amu

isotopic fractionations observed, matrix effects cannot lead to a significant shift in the reported $\Delta^{17}\text{O}$ values. A general correction factor (of magnitude less than our reported uncertainties) was applied to all measurements, which accounts for IMF and differences in detector efficiency. Since this is smaller than the typical analytical precision achieved for a given spot, we follow the approach taken by studies employing conventional SIMS, e.g. (3-5), and we neglect second order mineral specific corrections.

Oxygen isotope compositions are reported in terms of $\delta^{17}\text{O}$ and $\delta^{18}\text{O}$ relative to standard mean ocean water (SMOW, see Table S1). These values reflect the per mil difference from the composition of SMOW such that $\delta^i\text{O}_{\text{SMOW}} = 10^3((^i\text{O}/^{16}\text{O})/(^i\text{O}/^{16}\text{O})_{\text{SMOW}} - 1)$ where i refers to either 17 or 18. The primary standard material used in all analytical sessions was Burma spinel, which is $\sim 6\text{‰}$ per amu heavier than SMOW. Based on replicate analyses of the spinel, the external precision for mass dependent fractionation was $\sim 5.0\text{‰}$ (2 SD) per amu (comparable to that obtained by the NanoSIMS at NASA Johnson Space Center (2)). $\Delta^{17}\text{O}$ defined as $\Delta^{17}\text{O} = \delta^{17}\text{O} - 0.52\delta^{18}\text{O}$ represents the departure from the terrestrial mass fractionation (TMF) line that defines the terrestrial oxygen reservoir. The reported uncertainty accounts for both the internal measurement precision on an individual analysis and the reproducibility obtained for repeated measurements of the standards, estimated by the standard deviation in both $\delta^{17}\text{O}$ and $\delta^{18}\text{O}$. Based on replicate analyses of the two terrestrial standards (Burma spinel, $n=12$ and Miakejima anorthite, $n=6$), measured during multiple sessions, our precision for $\Delta^{17}\text{O}$ ranged from 2.5 to 3.4‰ (2 SD), respectively. The apparent difference between average $\Delta^{17}\text{O}$ values of the two terrestrial mineral standards was $<0.5\text{‰}$. The reported uncertainty for individual $\Delta^{17}\text{O}$ measurements include the overall reproducibility (2.8‰, 2 SD) measured for both terrestrial standards. A majority of the sample measurements come from spots spaced every $\sim 7\text{--}10\text{ }\mu\text{m}$ along continuous traverses across the WL rim and the outer $\sim 150\text{ }\mu\text{m}$ of the massive melilite interior (Fig. S4). An additional traverse (Traverse #3) was constructed retroactively for data collected in a less regular fashion across the exterior of A37 and surrounding rim in the region indicated in Fig. 1, by “projecting” the spot analyses on to a plane. The remaining measurements were made within and around the “micro-CAI”. Because our analytical procedure is somewhat unconventional for the

NanoSIMS (i.e., employing a relatively large primary beam and mixed detector types) the long-term ability to obtain the reported high precision uncertainty remains to be tested.

At the University of Chicago selected areas of the sample were documented with a JEOL JSM-5800LV scanning electron microscope, and wavelength-dispersive (WDS) analyses were obtained with a Cameca SX-50 electron microprobe operated at 15 kV. The WDS data were reduced using the modified ZAF correction procedure PAP (6). The melilite zoning data are reported in Table S2 and representative mineral compositions for the WL phases are included in Table S3. At LLNL high-resolution backscattered electron images (BSE) and digital x-ray maps were obtained with JEOL 7401-F and FEI Inspect F field emission scanning electron microscopes, respectively. The latter is equipped with an EDAX Apollo 40 energy-dispersive x-ray microanalysis system and imaging software that was used to study compositional zoning and to make the elemental maps.

Sample Material: A polished thick section of the inclusion A37 was studied petrographically (both optically and by scanning electron microscopy, including BSE and x-ray mapping). A37 is an ~7x4 mm compact Type A CAI composed primarily of melilite (Åk_{20-40}), 20-70 μm -sized spinel, anhedral perovskite, rare fassaite and rhönite that are often found in between melilite grains; see (7, 8) for greater detail. Common to some igneous Type A CAIs, A37 shows evidence for fractional crystallization of melilite analogous to the mantles of Type B1 CAIs. Individual melilite grains in A37 are slightly zoned in composition and exhibit polygonal cross sections. In this orientation, they exhibit triple junctions at grain boundaries (i.e., in the interior where three grains meet) that can be seen in the Al x-ray map shown in Fig. S1.

A37 is mantled by a ~50 to 100 μm thick Wark-Lovering (WL) rim composed from its interior outwards of hibonite, spinel (often enclosing perovskite), melilite/sodalite, Ti-bearing pyroxene, Al-rich pyroxene, and an outermost band of forsterite. The forsterite may have accreted (as an accretionary rim) onto the outside, rather than growing along with the other rim phases. An ~1 to 5 μm thick intermittent zone of melilite at the interface between the gehlenitic interior and the WL rim is relatively åkermanite-rich and Na-poor (Fig. S2). A small, spinel-rich, perovskite-bearing “micro-CAI” is observed within the WL rim and therefore likely co-existed with A37 during rim formation. Although interpretation of such observations is beyond the scope

of this contribution, the latter implies that in some regions of the solar nebula, CAIs of various sizes may have existed together prior to chondrite accretion.

Evidence for alteration is uncommon in A37 (7, 9). The rare exception includes localized secondary minerals, e.g., sodalite. Unlike some other Allende CAIs, most cracks and holes in A37 do not contain Na-bearing secondary phases (7). Some minerals in the interior of the inclusion have microscopic evidence of post-crystallization shock. These textures were studied by earlier investigations using transmission electron microscopy and secondary electron microscopy (9). These shock features could be partly due to passage of the CAIs through shock waves in the protoplanetary disk (i.e., micro-impacts) and/or during impacts on the chondrite parent body.

Science Online Materials:

Oxygen Isotope Compositions: Individual three-isotope plots of oxygen measured in the melilite interior, micro-CAI, WL rim, and rim shown with secondary minerals are included here so that mineral specific trends and petrographic affinities may be observed (Fig. S3A-D). Linear regressions calculated by Isoplot (10) are fit to the melilite interior and the WL rim data, respectively. In this case, assuming that the analytical errors are the only reason that the data scatter about the line (11) is probably not appropriate. Rather, the source of scatter within each data set likely includes a mixture of phenomena, both analytical and natural (“geological”). Therefore, the fit used herein assigns equal weight and zero error-correlations to each point. The slopes defined by linear regression of the melilite data (0.89 ± 0.06 2σ , MSWD=1.8, $n=45$) from the interior of A37 and a regression of data from various minerals in the surrounding WL rim (0.96 ± 0.05 2σ , MSWD=2.5, $n=65$) are both within error of the ~ 0.94 CCAM line (12).

Plotted on Fig. S3C are the data from the micro-CAI and the interior melilite. The micro-CAI appears to mimic the data trend from the larger CAI. The data that come from the interior of the micro-CAI (mainly perovskite and spinel) lie close to the CCAM slope (like the melilite interior spots described above). Fig. S3D shows all of the WL rim data including several sodalite measurements. All sodalite spots clearly fall on or near the TMF line implying a late-stage planetary origin.

Chemical Zoning of Melilite Interior: The O isotope zoning (Fig. 3) of A37 is contained within the outermost grains and unrelated to its chemical zoning (Fig. S1). The chemical variation of melilite in the interior of A37 is typical of igneous zoning (8). The Mg content increases inward from the margin (Fig. 4), reflecting inward crystallization during cooling, consistent with the compositional evolution for melilite produced by fractional crystallization of a molten condensate (13). Compositional zoning from gehlenitic (Al-rich) melilite at the edge to åkermanitic (Mg-rich) melilite in the interior matches experimental work (14). It is also consistent with trace element trends in many coarse-grained CAIs (15, 16) that provide evidence of an igneous origin. An alternative explanation is one in which Mg-evaporation-induced nucleation of low-Åk melilite forms at the edge of the CAI while it was a molten droplet (17). This is more difficult to reconcile with the high concentration of Na observed at the outer edge of A37 (Fig. 4).

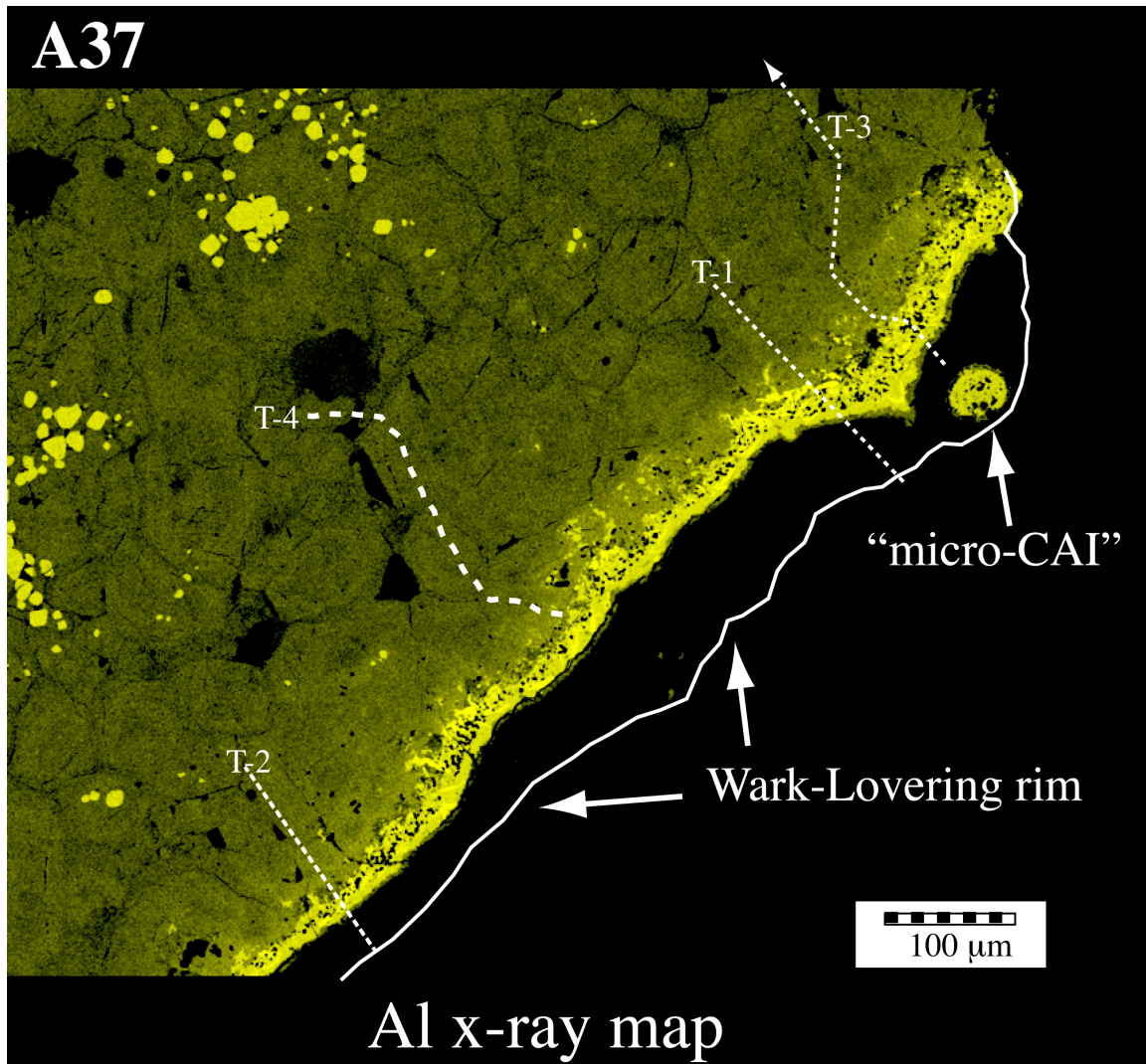


Fig. S1. Aluminum x-ray map with analytical traverses shown. The systematic variation in oxygen isotopes at the exterior of A37 is contained within the outermost grains, cf. (18). The oxygen isotope traverses span different sized grains, grain boundaries and zoning within grains. The zoning is characteristic of the exterior of the CAI and not specifically to individual crystals. Analyses taken from the interior of A37 show little variability.

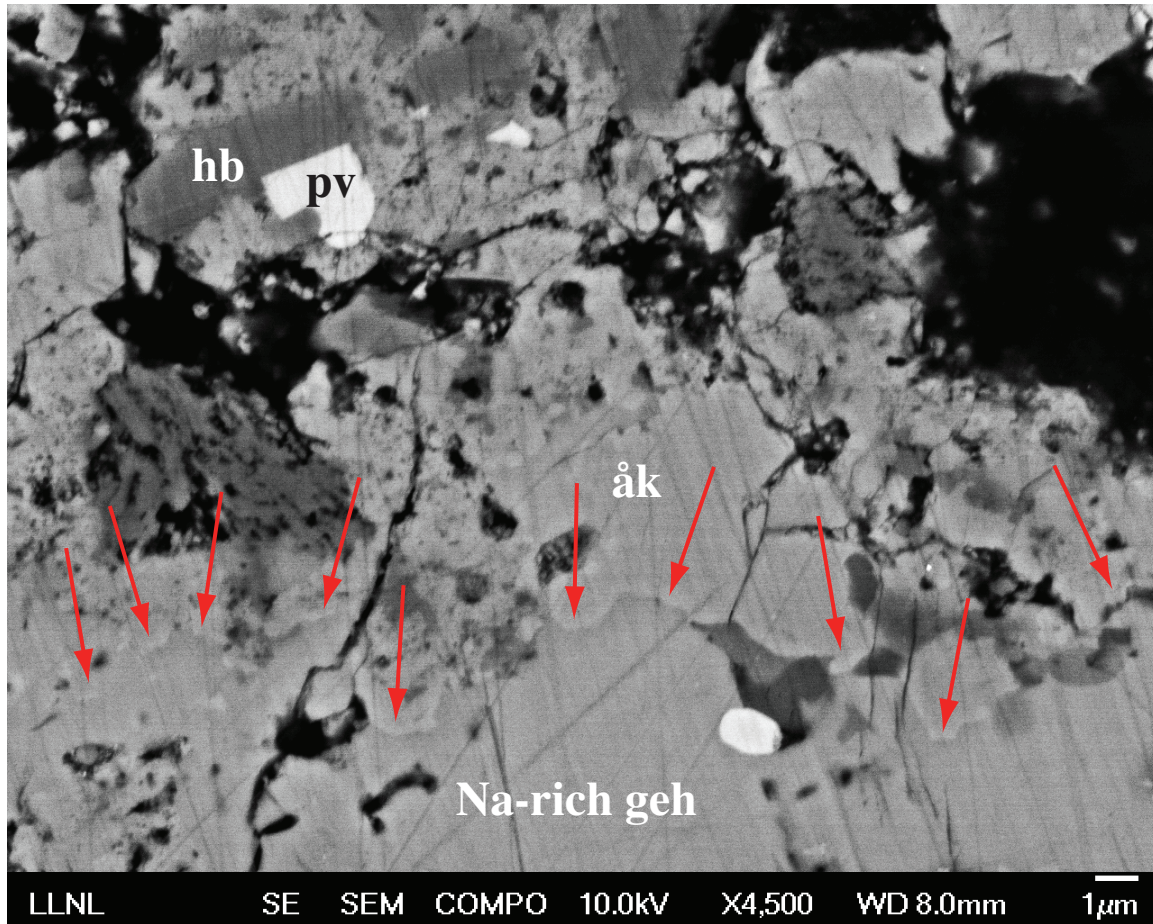


Fig. S2. Backscattered electron (BSE) image of interface between the gehlenitic interior (bottom) and the rim (top). This thin, outer, relatively åkermanite-rich and Na-poor melilite zone may represent the initiation of Wark-Lovering rim growth. Minerals are labeled in image as follows: hb=hibonite, pv=perovskite, åk=åkermanitic melilite, and geh=gehlenitic melilite. Semi-quantitative EDS spot analyses were used to document a sharp boundary in BSE image (marked by red arrows) between relative abundances of Na and Mg in melilite (i.e., Na-rich gehlenite vs. Na-poor åkermanite). The planetary-like oxygen isotopic composition of the thin åkermanitic melilite zone appears to record the transfer of CAIs from an ^{16}O -rich astrophysical setting to region(s) of relatively high pressure (where WL rims grow e.g. (19)) that contains nebular gas of varying oxygen composition.

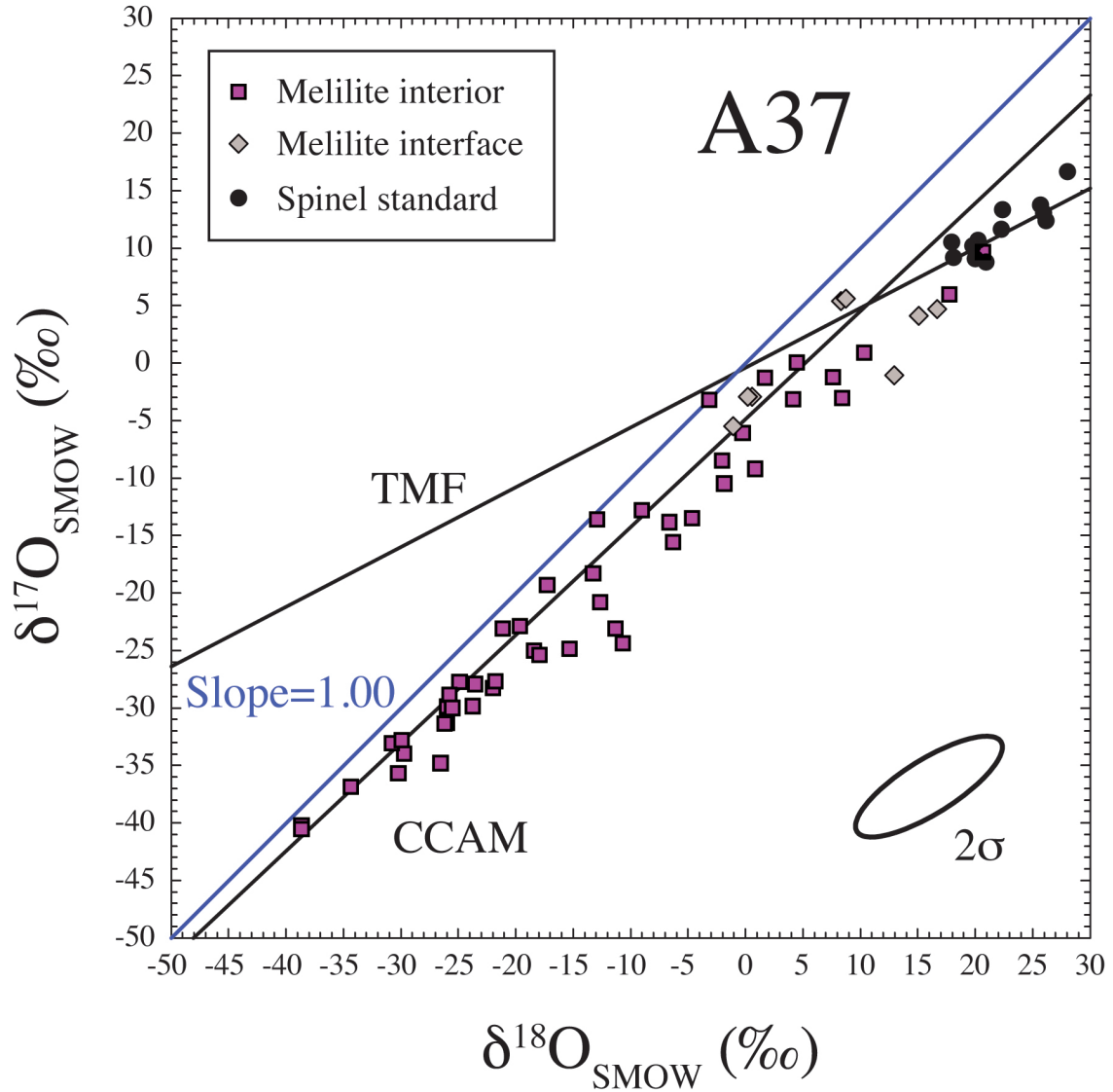


Fig. S3A. Three-isotope plot of oxygen measured in the melilite interior and at the interface with the WL rim of A37 that define a slope of 0.89 ± 0.06 2σ (MSWD=1.8, $n=45$). Melilite analyses tend to cluster more tightly along the more ^{16}O -rich part of the CCAM line and spread more widely towards planet-like oxygen compositions. A difference between the melilite and minerals in the surrounding WL rim (see Fig. S3B) can be seen by comparison. Error ellipse represents 2σ external reproducibility of terrestrial spinel standard.

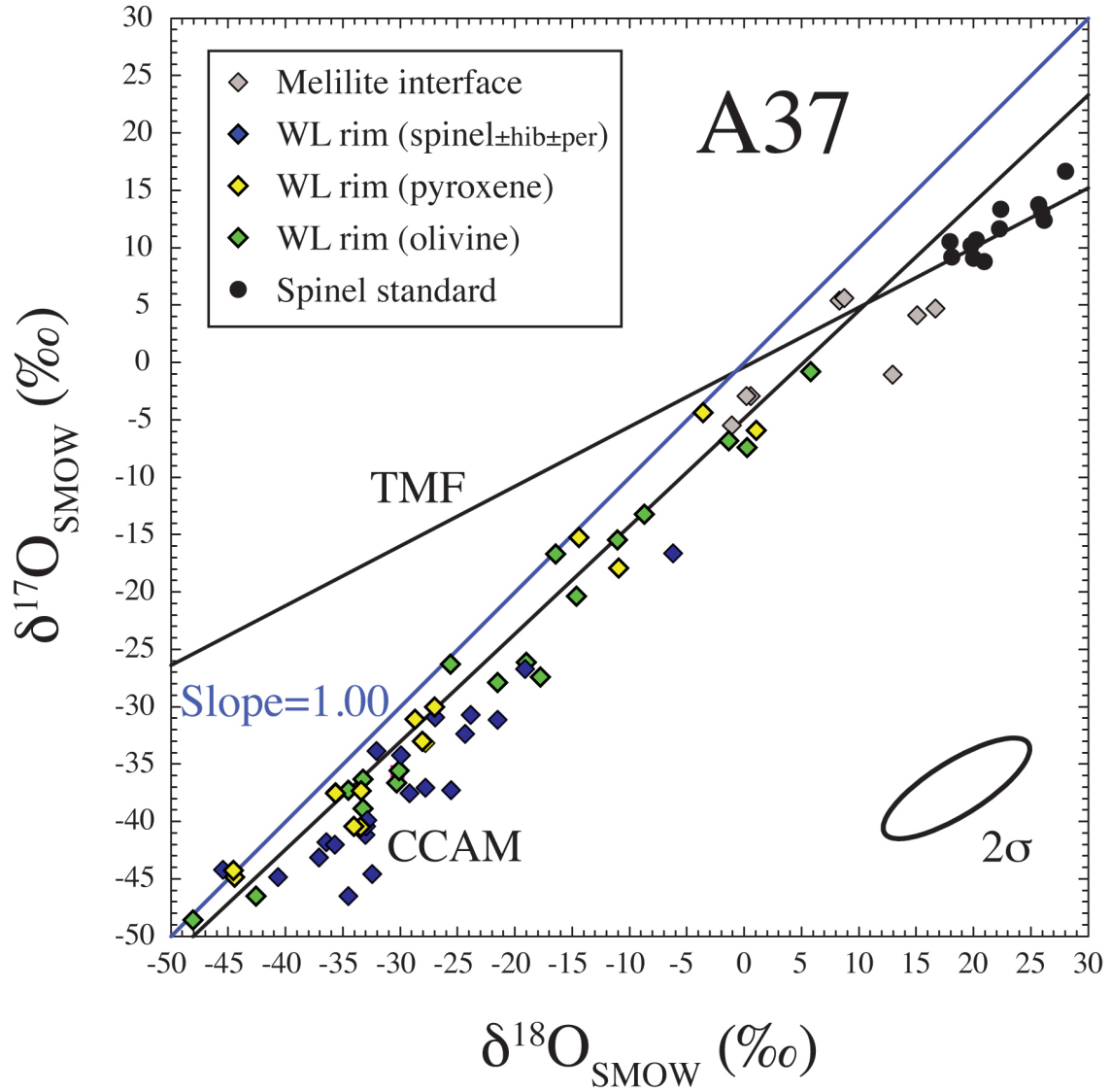


Fig. S3B. Three-isotope plot of oxygen measured in WL rim that define a slope of 0.96 ± 0.05 2σ (MSWD=2.5, n=65). The ^{16}O -rich spinel measurements appear to play a significant role on the relatively steep slope. Error ellipse represents 2σ external reproducibility of terrestrial spinel standard.

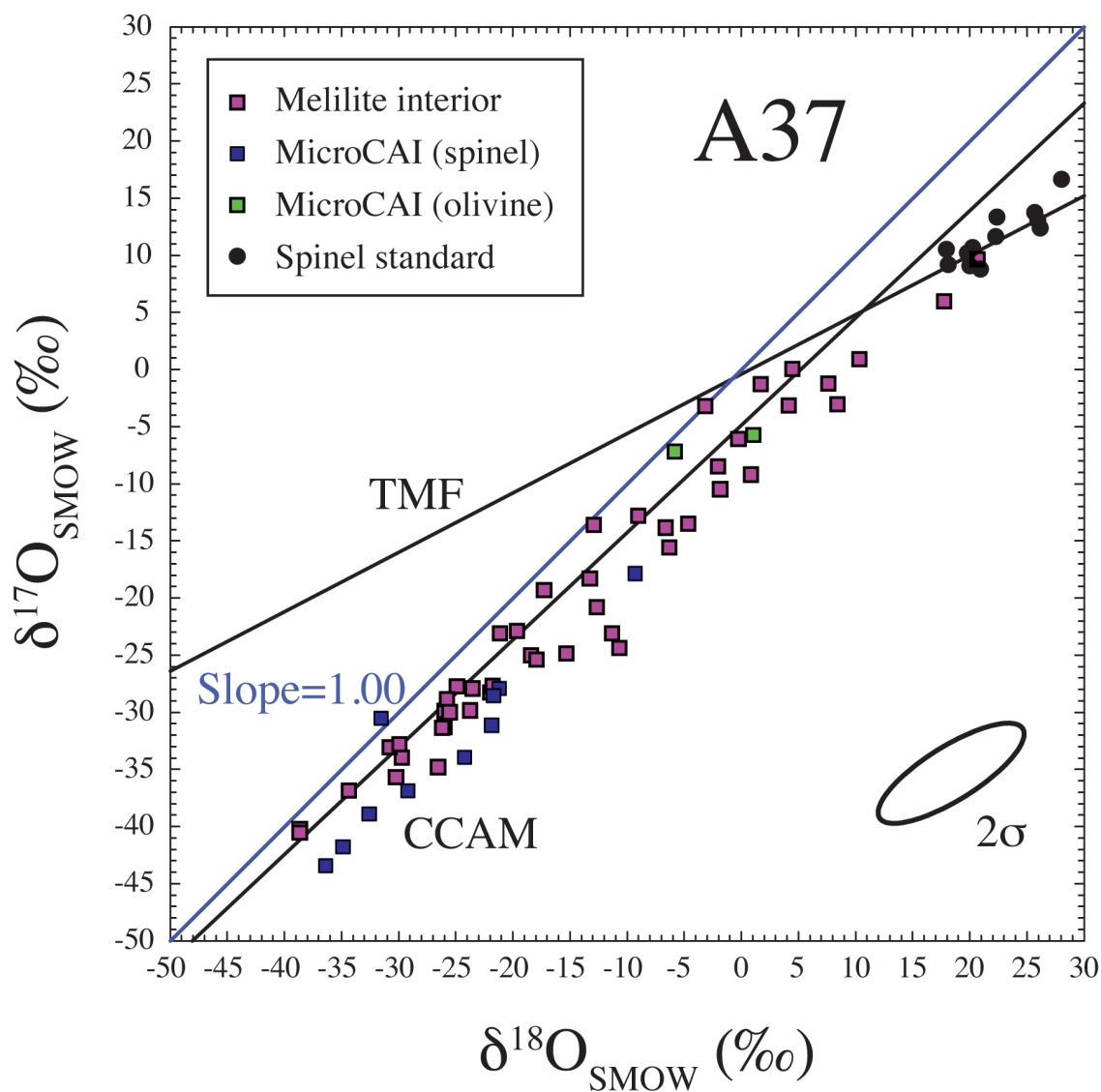


Fig. S3C. Three-isotope plot of oxygen measured in the micro-CAI that appears to mimic the data from A37. The interior analyses of the micro-CAI (mainly perovskite and spinel) lie along the CCAM line (like the melilite interior spots of A37). Olivine points are similar to WL rim olivine analyses. Error ellipse represents 2 σ external reproducibility of terrestrial spinel standard.

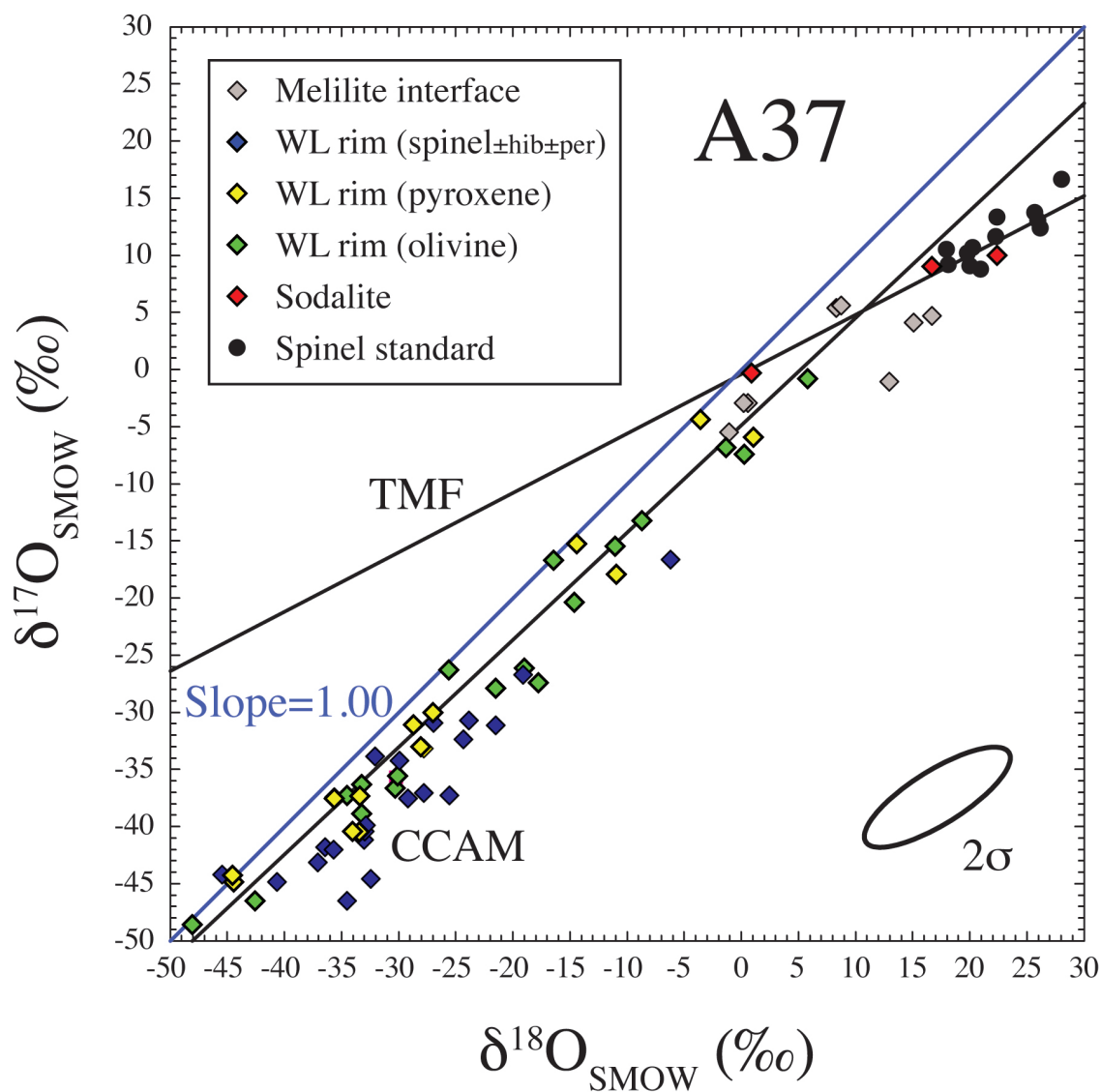


Fig. S3D. Three-isotope plot of oxygen measured in WL rim along with secondary minerals (several sodalite measurements). All sodalite spots clearly fall on the TMF line attesting to its late-stage origin. Error ellipse represents 2σ external reproducibility of terrestrial spinel standard.

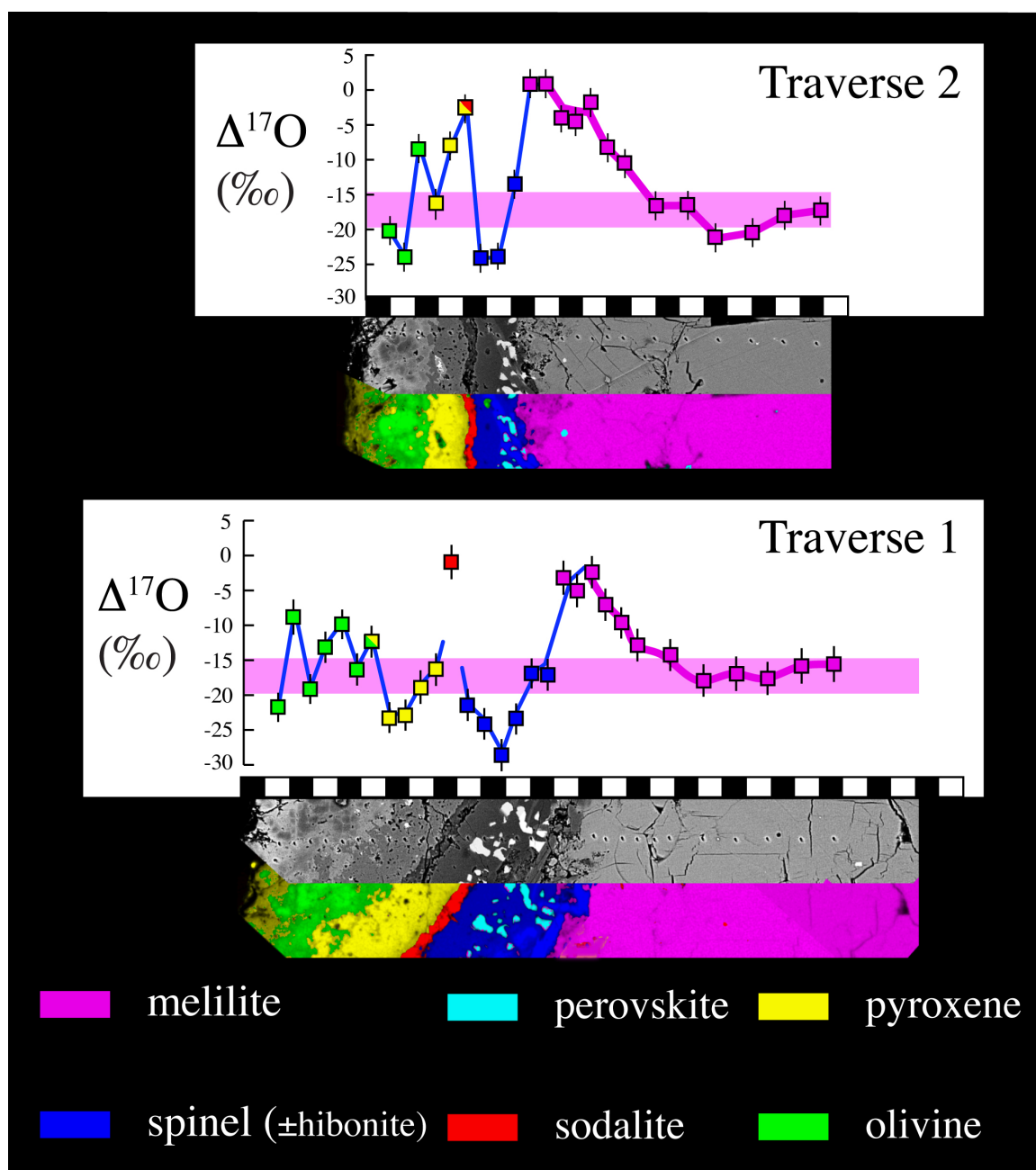


Fig. S4. Oxygen isotope zoning typical of A37 defined by ion microprobe Traverses 1, 2, and projected Traverse 3 (not shown). Analytical spot size smaller than width of symbols and can be seen in companion SEM images. BSE (gray scale) and x-ray mapping (mineral color-coding as in Fig. 1), respectively, accompany the oxygen data.

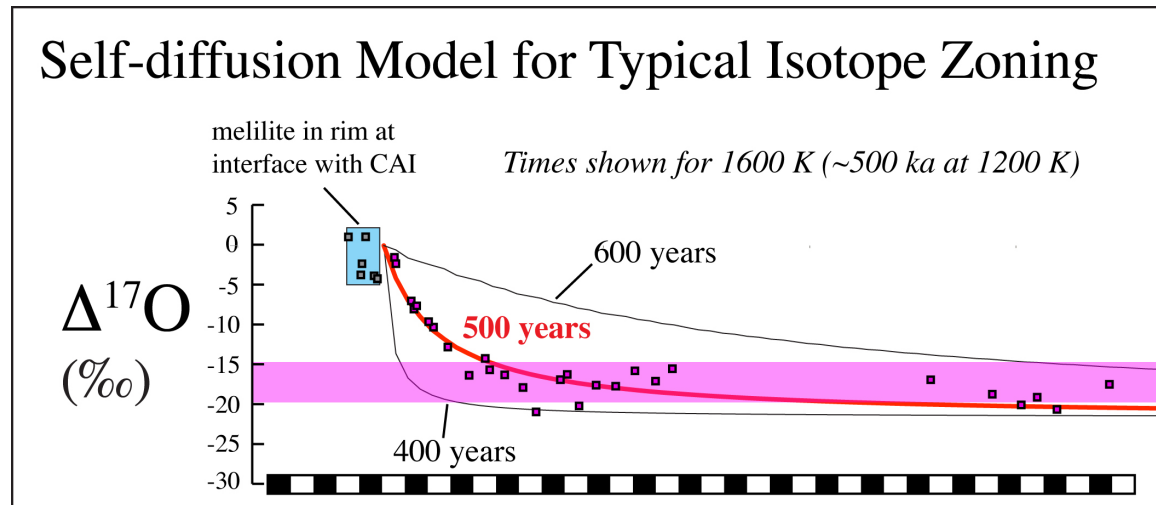


Fig. S5. Oxygen self-diffusion models compared to the isotope zoning typical of A37, which is defined by ion microprobe Traverses. Data of ^{16}O -poor, åkermanite-rich melilite adjacent to the somewhat irregular interface of the gehlenitic melilite margin of the CAI come from a zone that is less than 20 micrometers wide (i.e., blue box). Black and white scale bars = 10 μm per increment. Horizontal band $\Delta^{17}\text{O} = -15$ to -20 is representative of the interior.

References for *Science* Online Materials

1. R. N. Clayton, T. K. Mayeda, *Earth and Planetary Science Letters* **67**, 151 (1984).
2. M. Ito, S. Messenger, *Applied Surface Science* **255**, 1446 (2008).
3. S. S. Russell, G. J. MacPherson, L. A. Leshin, K. D. McKeegan, *Earth and Planetary Science Letters* **184**, 57 (2000).
4. K. D. McKeegan, L. A. Leshin, S. S. Russell, G. J. MacPherson, *Science* **280**, 414 (1998).
5. M. Ito, H. Nagasawa, H. Yurimoto, *Geochimica et Cosmochimica Acta* **68**, 2905 (2004).
6. J. L. Pouchou, F. Pichoir, *Rech. Aerosp.* **3**, 13 (1984).
7. A. Bischoff, H. Palme, B. Spettel, in *Lunar and Planetary Science Conference XVIII*. (1987), pp. 81-82.
8. S. B. Simon, A. M. Davis, L. Grossman, *Geochimica et Cosmochimica Acta* **63**, 1233 (1999).
9. A. Greshake, A. Bischoff, A. Putnis, *Meteoritics & Planetary Science* **33**, 75 (1998).
10. K. R. Ludwig. (Berkeley Geochronology Center, Berkeley, CA, USA, 2003), pp. A Geochronological Toolkit for Microsoft Excel.
11. D. York, *Earth and Planetary Science Letters* **5**, 320 (1969).
12. R. N. Clayton, N. Onuma, L. Grossman, T. K. Mayeda, *Earth and Planetary Science Letters* **34**, 209 (1977).
13. G. J. MacPherson, L. Grossman, *Earth and Planetary Science Letters* **52**, 16 (1981).
14. E. F. Osborn, J. F. Schairer, *American Journal of Science* **239**, 715 (1941).
15. S. M. Kuehner, J. R. Laughlin, L. Grossman, M. L. Johnson, D. S. Burnett, *Geochimica et Cosmochimica Acta* **53**, 3115 (1989).
16. J. R. Beckett, A. J. Spivack, I. D. Hutcheon, G. J. Wasserburg, E. Stolper, *Geochimica et Cosmochimica Acta* **54**, 1755 (1990).
17. F. M. Richter, R. A. Mendybaev, A. M. Davis, *Meteoritics & Planetary Science* **41**, 83 (2006).
18. H. Yurimoto, M. Morioka, H. Nagasawa, *Geochimica et Cosmochimica Acta* **53**, 2387 (1989).
19. J. I. Simon *et al.*, *Earth and Planetary Science Letters* **238**, 272 (2005).

Table S1. Oxygen Isotope Compositions

Spot Name	Material	Distance (µm) from WL-interior interface	¹⁷ O/ ¹⁶ O measured	SE (%)	δ ¹⁷ O/‰ IMF corrected	SE	¹⁸ O/ ¹⁶ O measured	SE (%)	δ ¹⁸ O/‰ IMF corrected	SE	Δ ¹⁷ O	SE	Si/ ²⁸ O	SE (%)
Traverse-1														
T-1 s26	olivine clear of edge	-290	3.6876E-04	1.45E-01	-38.9	2.7	1.9377E-03	6.89E-02	-33.3	3.5	-21.6	2.1	9.8E-04	0.5
T-1 s27	olivine appears more Faylitic	-277	3.7860E-04	1.66E-01	-13.2	2.8	1.9870E-03	1.13E-01	-8.7	3.6	-8.7	2.4	1.0E-03	0.8
T-1 s28	olivine appears more Forsteritic	-270	3.6932E-04	1.49E-01	-37.4	2.7	1.9330E-03	6.76E-02	-35.6	3.5	-18.9	2.1	1.1E-03	0.5
T-1 s29	olivine slightly more faylitic	-260	3.7360E-04	1.53E-01	-26.3	2.8	1.9530E-03	8.18E-02	-25.6	3.5	-12.9	2.2	1.1E-03	0.8
T-1 s30	olivine more forsteritic	-249	3.7773E-04	1.38E-01	-15.5	2.7	1.9822E-03	7.92E-02	-11.1	3.5	-9.7	2.1	1.7E-03	0.9
T-1 s31	olivine fayalitic near pyroxene	-235	3.7366E-04	1.53E-01	-26.1	2.8	1.9663E-03	9.60E-02	-19.0	3.5	-16.2	2.3	1.5E-03	1.4
T-1 s32	pyroxene >olivine	-221	3.7679E-04	1.57E-01	-17.9	2.8	1.9825E-03	8.10E-02	-10.9	3.5	-12.3	2.2	2.0E-03	1.3
T-1 s33	pyroxene	-200	3.6815E-04	1.53E-01	-40.5	2.8	1.9373E-03	7.83E-02	-33.5	3.5	-23.1	2.2	1.8E-03	0.8
T-1 s34	pyroxene	-181	3.6817E-04	1.56E-01	-40.4	2.8	1.9361E-03	7.91E-02	-34.1	3.5	-22.7	2.2	1.6E-03	0.6
T-1 s35	pyroxene	-162	3.7096E-04	1.76E-01	-33.2	2.9	1.9487E-03	7.76E-02	-27.8	3.5	-18.7	2.3	1.8E-03	0.6
T-1 s36	pyroxene near sodalite	-151	3.7176E-04	1.68E-01	-31.1	2.8	1.9469E-03	7.46E-02	-28.7	3.5	-16.2	2.3	1.4E-03	0.7
T-1 s37	sodalite near crack > spinel	-137	3.8354E-04	1.72E-01	-0.3	2.9	2.0062E-03	8.32E-02	0.9	3.5	-0.8	2.4	2.2E-03	2.0
T-1 s38	spinel	-121	3.6670E-04	1.66E-01	-44.3	2.8	1.9152E-03	7.82E-02	-44.5	3.5	-21.1	2.2	6.9E-07	4.3
T-1 s39	spinel	-103	3.6789E-04	1.62E-01	-41.2	2.8	1.9382E-03	7.40E-02	-33.0	3.5	-24.0	2.2	4.0E-07	6.5
T-1 s40	spinel	-86	3.6585E-04	1.65E-01	-46.5	2.8	1.9352E-03	7.98E-02	-34.5	3.5	-28.5	2.2	4.7E-07	5.8
T-1 s41	spinel	-71	3.6817E-04	1.58E-01	-40.4	2.8	1.9383E-03	7.54E-02	-33.0	3.5	-23.3	2.2	1.7E-06	3.9
T-1 s42	perovskite> spinel	-56	3.7342E-04	1.49E-01	-26.7	2.7	1.9661E-03	6.96E-02	-19.1	3.5	-16.8	2.1	1.1E-05	1.8
T-1 s43	hibonite> spinel	-35	3.7181E-04	1.64E-01	-30.9	2.8	1.9504E-03	7.15E-02	-26.9	3.5	-16.9	2.2	1.7E-05	2.4
T-1 s44	melilite "rim"	-20	3.8253E-04	1.72E-01	-2.9	2.9	2.0048E-03	8.01E-02	0.2	3.5	-3.1	2.4	8.9E-04	0.6
T-1 s45	melilite "rim"	0	3.8155E-04	1.67E-01	-5.5	2.9	2.0022E-03	7.71E-02	-1.1	3.5	-4.9	2.3	1.1E-03	1.5
T-1 s46	melilite interior	13	3.8368E-04	1.57E-01	0.1	2.8	2.0134E-03	8.02E-02	4.5	3.5	-2.3	2.3	1.1E-03	0.7
T-1 s47	melilite interior	30	3.7846E-04	1.58E-01	-13.6	2.8	1.9785E-03	8.30E-02	-12.9	3.5	-6.9	2.3	1.2E-03	0.7
T-1 s48	melilite interior	48	3.8014E-04	1.49E-01	-9.2	2.8	2.0061E-03	8.12E-02	0.9	3.5	-9.6	2.2	1.1E-03	0.6
T-1 s49	melilite interior	60	3.7489E-04	1.64E-01	-22.9	2.8	1.9650E-03	8.30E-02	-19.6	3.5	-12.7	2.3	1.1E-03	0.7
T-1 s51	melilite interior	88	3.7570E-04	1.59E-01	-20.8	2.8	1.9790E-03	7.85E-02	-12.7	3.5	-14.2	2.2	1.1E-03	0.9
T-1 s52	melilite interior	125	3.7168E-04	1.65E-01	-31.3	2.8	1.9523E-03	8.01E-02	-26.0	3.5	-17.8	2.3	1.3E-03	0.7
T-1 s53	melilite interior	162	3.7284E-04	1.80E-01	-28.2	2.9	1.9603E-03	8.26E-02	-22.0	3.5	-16.8	2.4	1.1E-03	0.6
T-1 s54	melilite interior	196	3.7223E-04	1.65E-01	-29.8	2.8	1.9568E-03	9.07E-02	-23.7	3.5	-17.5	2.3	1.2E-03	0.7
T-1 s55	melilite interior	234	3.7297E-04	1.81E-01	-27.9	2.9	1.9572E-03	9.53E-02	-23.5	3.5	-15.7	2.4	1.3E-03	1.1
T-1 s56	melilite interior	269	3.7408E-04	1.87E-01	-25.0	3.0	1.9675E-03	8.80E-02	-18.4	3.5	-15.4	2.5	1.1E-03	0.5
Traverse 2														
T-2 s97	olivine near crack	-218	3.7004E-04	1.53E-01	-35.6	2.8	1.9441E-03	7.42E-02	-30.1	3.5	-19.9	2.2	1.1E-03	0.5
T-2 s98	olivine	-197	3.6504E-04	1.52E-01	-48.6	2.7	1.9080E-03	7.24E-02	-48.1	3.5	-23.6	2.1	9.6E-04	0.6
T-2 s99	olivine near pyroxene	-178	3.7727E-04	1.38E-01	-16.7	2.7	1.9714E-03	6.93E-02	-16.5	3.5	-8.1	2.1	9.8E-04	0.8
T-2 s100	pyroxene >olivine	-157	3.7216E-04	1.48E-01	-30.0	2.7	1.9503E-03	7.14E-02	-27.0	3.5	-16.0	2.1	1.5E-03	0.7
T-2 s101	pyroxene	-137	3.7781E-04	1.66E-01	-15.3	2.8	1.9755E-03	8.44E-02	-14.4	3.5	-7.8	2.3	2.6E-03	1.7
T-2 s102	pyroxene > sodalite	-117	3.8199E-04	1.64E-01	-4.4	2.8	1.9972E-03	7.26E-02	-3.6	3.5	-2.5	2.3	1.2E-03	0.5
T-2 s103	spinel	-100	3.6713E-04	1.67E-01	-43.1	2.8	1.9300E-03	7.79E-02	-37.1	3.5	-23.9	2.3	8.4E-07	5.8
T-2 s104	hibonite	-79	3.6649E-04	1.72E-01	-44.8	2.9	1.9229E-03	8.00E-02	-40.6	3.5	-23.7	2.3	3.7E-06	1.6
T-2 s105	spinel> melilite >per	-58	3.7729E-04	1.52E-01	-16.6	2.8	1.9920E-03	6.93E-02	-6.2	3.5	-13.4	2.2	3.7E-04	3.1
T-2 s106	melilite "rim"	-39	3.8573E-04	1.71E-01	5.4	2.9	2.0211E-03	8.33E-02	8.3	3.5	1.1	2.4	8.4E-04	0.6
T-2 s107	melilite "rim" on small crack	-20	3.8580E-04	1.72E-01	5.6	2.9	2.0219E-03	7.83E-02	8.7	3.5	1.0	2.4	3.2E-03	0.9
T-2 s108	melilite "rim" (or reacted interior)	0	3.8545E-04	1.64E-01	4.7	2.9	2.0378E-03	8.11E-02	16.7	3.5	-4.0	2.3	1.4E-03	0.6
T-2 s109	melilite	20	3.8401E-04	1.64E-01	0.9	2.8	2.0251E-03	7.75E-02	10.3	3.5	-4.5	2.3	1.1E-03	0.6
T-2 s110	melilite	40	3.8243E-04	1.55E-01	-3.2	2.8	1.9981E-03	7.44E-02	-3.1	3.5	-1.6	2.2	1.2E-03	0.7
T-2 s111	melilite	60	3.7876E-04	1.60E-01	-12.8	2.8	1.9863E-03	7.54E-02	-9.0	3.5	-8.1	2.2	1.2E-03	0.7
T-2 s112	melilite	80	3.7627E-04	1.57E-01	-19.3	2.8	1.9698E-03	7.81E-02	-17.3	3.5	-10.3	2.2	1.3E-03	0.8
T-2 s113	melilite	120	3.7222E-04	1.60E-01	-29.9	2.8	1.9523E-03	7.74E-02	-26.0	3.5	-16.4	2.2	1.2E-03	0.6
T-2 s114	melilite	160	3.7306E-04	1.68E-01	-27.7	2.8	1.9607E-03	8.44E-02	-21.8	3.5	-16.3	2.3	1.3E-03	0.8
T-2 s115	melilite	199	3.7033E-04	1.68E-01	-34.8	2.8	1.9512E-03	7.63E-02	-26.5	3.5	-21.0	2.3	1.3E-03	0.7
T-2 s116	melilite	239	3.6825E-04	1.65E-01	-40.2	2.8	1.9269E-03	7.99E-02	-38.6	3.5	-20.1	2.3	1.3E-03	0.8
T-2 s117	melilite	278	3.7165E-04	1.82E-01	-31.3	2.9	1.9519E-03	8.42E-02	-26.2	3.5	-17.7	2.4	1.3E-03	0.6
T-3 s118	melilite	318	3.7100E-04	1.83E-01	-33.0	2.9	1.9427E-03	8.21E-02	-30.8	3.5	-17.0	2.4	1.3E-03	0.8
Traverse-3 (projection)														
T-3 s10	olivine	-271	3.6585E-04	1.52E-01	-46.5	2.7	1.9190E-03	6.89E-02	-42.6	3.5	-24.3	2.1	1.2E-03	0.8
T-3 s9	olivine	-251	3.8105E-04	1.57E-01	-6.8	2.8	2.0017E-03	7.30E-02	-1.3	3.5	-6.1	2.2	1.1E-03	0.5
T-3 s20	olivine	-243	3.7297E-04	1.67E-01	-27.9	2.8	1.9613E-03	1.03E-01	-21.5	3.5	-16.7	2.4	1.7E-03	1.3
T-3 s8	olivine	-223	3.8082E-04	1.56E-01	-7.4	2.8	2.0049E-03	7.91E-02	0.3	3.5	-7.5	2.2	9.4E-04	0.6
T-3 s7	pyroxene	-197	3.7102E-04	1.91E-01	-33.0	3.0	1.9481E-03	9.01E-02	-28.1	3.5	-18.4	2.5	1.7E-03	0.9
T-3 s18	pyroxene	-191	3.6670E-04	1.71E-01	-44.3	2.8	1.9151E-03	7.78E-02	-44.5	3.5	-21.1	2.3	2.0E-03	0.8
T-3 s6	pyroxene	-173	3.8140E-04	1.67E-01	-5.9	2.9	2.0065E-03	8.07E-02	1.1	3.5	-6.4	2.3	2.0E-03	1.0
T-3 s17	spinel	-155	3.6673E-04	1.62E-01	-44.2	2.8	1.9133E-03	7.52E-02	-45.4	3.5	-20.6	2.2	8.3E-05	2.1
T-3 s2	spinel near sodalite	-151	3.7189E-04	1.92E-01	-30.7	3.0	1.9566E-03	9.07E-02	-23.8	3.5	-18.3	2.5	3.4E-04	4.2
T-3 s4	spinel	-151	3.6658E-04	1.80E-01	-44.6	2.9	1.9394E-03	1.00E-01	-32.4	3.5	-27.7	2.4	4.3E-05	4.6
T-3 s3	spinel	-144	3.6756E-04	1.71E-01	-42.0	2.8	1.9328E-03</							

Traverse-5 (between 1 and 2)												
T-5 s60	olivine more Fay	-291	3.8335E-04	1.33E-01	-0.8	2.7	2.0160E-03	6.30E-02	5.8	3.5	-3.8	2.0 9.4E-04 0.9
T-5 s61	olivine more Fo	-276	3.6963E-04	1.58E-01	-36.6	2.8	1.9436E-03	7.47E-02	-30.3	3.5	-20.9	2.2 1.0E-03 0.9
T-5 s62	olivine more Fo	-258	3.7315E-04	1.47E-01	-27.4	2.7	1.9688E-03	7.02E-02	-17.8	3.5	-18.2	2.1 1.1E-03 0.7
T-5 s63	olivine more Fo near hairline crack	-243	3.6939E-04	1.52E-01	-37.2	2.8	1.9352E-03	6.88E-02	-34.5	3.5	-19.3	2.1 1.2E-03 0.9
T-5 s64	olivine more Fay	-222	3.6974E-04	1.65E-01	-36.3	2.8	1.9378E-03	8.81E-02	-33.2	3.5	-19.1	2.3 1.1E-03 0.8
T-5 s65	olivine > pyroxene	-208	3.7585E-04	1.71E-01	-20.4	2.9	1.9751E-03	8.78E-02	-14.6	3.5	-12.8	2.4 1.2E-03 1.0
T-5 s67	pyroxene near crack	-167	3.6648E-04	1.72E-01	-44.8	2.9	1.9153E-03	7.18E-02	-44.4	3.5	-21.7	2.3 1.9E-03 0.9
T-5 s68	pyroxene	-148	3.6928E-04	1.57E-01	-37.5	2.8	1.9330E-03	7.43E-02	-35.6	3.5	-19.0	2.2 2.0E-03 1.2
T-5 s69	pyroxene near sodalite	-128	3.6935E-04	1.50E-01	-37.4	2.7	1.9374E-03	7.34E-02	-33.4	3.5	-20.0	2.1 1.9E-03 0.9
T-5 s70	spinel> sodalite	-110	3.7055E-04	1.80E-01	-34.2	2.9	1.9444E-03	9.08E-02	-29.9	3.5	-18.7	2.4 1.8E-04 0.7
T-5 s71	spinel	-95	3.7172E-04	1.69E-01	-31.2	2.8	1.9613E-03	7.48E-02	-21.5	3.5	-20.0	2.3 7.4E-07 5.2
T-5 s72	spinel	-81	3.6947E-04	1.73E-01	-37.0	2.9	1.9487E-03	8.25E-02	-27.8	3.5	-22.6	2.3 2.8E-06 2.2
T-5 s73	spinel	-71	3.6938E-04	1.75E-01	-37.3	2.9	1.9531E-03	8.06E-02	-25.6	3.5	-24.0	2.3 7.2E-07 4.0
T-5 s74	hibonite >spinel	-55	3.6764E-04	1.80E-01	-41.8	2.9	1.9314E-03	8.23E-02	-36.4	3.5	-22.9	2.4 3.5E-06 2.1
T-5 s75	hibonite near crack	-38	3.7068E-04	1.72E-01	-33.9	2.9	1.9401E-03	8.69E-02	-32.1	3.5	-17.2	2.3 1.7E-04 3.9
T-5 s76	Si and Ca rich unknown phase	-17	3.8524E-04	1.61E-01	4.1	2.8	2.0347E-03	7.53E-02	15.1	3.5	-3.7	2.3 1.1E-03 0.7
T-5 s77	melilit> spinel "rim"	0	3.6895E-04	1.90E-01	-38.4	3.0	1.9342E-03	8.30E-02	-35.0	3.5	-20.2	2.4 1.1E-04 0.4
T-5 s78	melilit interior	19	3.8245E-04	1.71E-01	-3.2	2.9	2.0127E-03	8.90E-02	4.1	3.5	-5.3	2.4 1.6E-03 2.7
T-5 s79	melilit interior	38	3.8595E-04	1.67E-01	6.0	2.9	2.0400E-03	7.96E-02	17.8	3.5	-3.3	2.3 9.5E-04 1.0
T-5 s81	melilit interior	80	3.8318E-04	1.62E-01	-1.3	2.8	2.0078E-03	7.46E-02	1.7	3.5	-2.1	2.3 2.0E-03 0.7
T-5 s82	melilit interior	95	3.8319E-04	1.66E-01	-1.2	2.9	2.0197E-03	7.36E-02	7.6	3.5	-5.2	2.3 1.5E-03 0.8
T-5 s83	melilit interior	121	3.8735E-04	1.60E-01	9.6	2.8	2.0459E-03	7.13E-02	20.7	3.5	-1.1	2.3 1.5E-03 0.7
T-5 s84	melilit interior	140	3.8134E-04	1.70E-01	-6.1	2.9	2.0039E-03	8.36E-02	-0.2	3.5	-5.9	2.3 1.4E-03 0.8
T-5 s86	Per > melilit	233	3.7482E-04	1.34E-01	-23.1	2.7	1.9620E-03	6.80E-02	-21.1	3.5	-12.1	2.0 1.3E-04 1.8
T-5 s87	melilit interior	250	3.7836E-04	1.71E-01	-13.8	2.9	1.9911E-03	8.53E-02	-6.6	3.5	-10.4	2.4 1.1E-03 0.6
T-5 s88	melilit interior	270	3.7965E-04	1.72E-01	-10.5	2.9	2.0007E-03	8.69E-02	-1.8	3.5	-9.5	2.4 1.5E-03 0.9
T-5 s89	melilit interior	290	3.7849E-04	1.68E-01	-13.5	2.9	1.9951E-03	8.71E-02	-4.6	3.5	-11.1	2.3 2.2E-03 2.8
T-5 s90	melilit interior	308	3.7665E-04	1.78E-01	-18.3	2.9	1.9778E-03	8.48E-02	-13.3	3.5	-11.4	2.4 1.4E-03 0.7
T-5 s91	melilit interior	328	3.7769E-04	1.67E-01	-15.6	2.9	1.9918E-03	8.46E-02	-6.3	3.5	-12.3	2.3 1.6E-03 0.9
T-5 s92	melilit interior	366	3.7304E-04	1.78E-01	-27.7	2.9	1.9545E-03	1.01E-01	-24.9	3.5	-14.8	2.4 2.9E-03 1.1
T-5 s93	melilit interior	405	3.7481E-04	1.86E-01	-23.1	3.0	1.9817E-03	8.30E-02	-11.3	3.5	-17.2	2.4 1.4E-03 0.7
T-5 s94	melilit interior	441	3.7432E-04	1.61E-01	-24.4	2.8	1.9830E-03	7.70E-02	-10.7	3.5	-18.8	2.2 1.6E-03 0.7
T-5 s95	melilit interior	480	3.7414E-04	1.73E-01	-24.9	2.9	1.9737E-03	7.96E-02	-15.3	3.5	-16.9	2.3 1.4E-03 0.7
"Micro-CAI"												
MCAI s21	spinel	interior	3.7067E-04	1.63E-01	-33.9	2.8	1.9558E-03	7.92E-02	-24.2	3.5	-21.3	2.2 6.5E-04 1.4
MCAI s22	spinel	interior	3.6954E-04	1.78E-01	-36.9	2.9	1.9459E-03	8.22E-02	-29.2	3.5	-21.7	2.4 2.3E-04 4.4
MCAI s23	spinel	interior	3.7298E-04	1.78E-01	-27.9	2.9	1.9619E-03	8.62E-02	-21.2	3.5	-16.9	2.4 7.3E-04 1.0
MCAI s121	pyroxene	near edge	3.7273E-04	2.00E-01	-28.5	3.0	1.9609E-03	1.24E-01	-21.7	3.6	-17.3	2.7 2.1E-03 1.3
MCAI s122	pyroxene near olivine	near edge	3.6876E-04	1.72E-01	-38.9	2.9	1.9391E-03	7.70E-02	-32.6	3.5	-22.0	2.3 2.1E-03 0.9
MCAI s123	olivine	near edge	3.7198E-04	1.84E-01	-30.5	2.9	1.9412E-03	1.02E-01	-31.5	3.5	-14.1	2.5 2.0E-03 1.1
MCAI s124	olivine> spinel	near edge	3.8147E-04	1.78E-01	-5.7	2.9	2.0065E-03	8.70E-02	1.1	3.5	-6.3	2.4 1.3E-03 0.9
MCAI s125	spinel	interior	3.6767E-04	1.89E-01	-41.7	3.0	1.9345E-03	8.88E-02	-34.9	3.5	-23.6	2.4 5.3E-07 5.8
MCAI s126	spinel	interior	3.7174E-04	1.82E-01	-31.1	2.9	1.9606E-03	8.61E-02	-21.8	3.5	-19.8	2.4 2.9E-04 2.3
MCAI s127	spinel	interior	3.6540E-04	1.81E-01	-47.7	2.9	1.8987E-03	8.95E-02	-52.7	3.5	-20.3	2.4 5.0E-07 5.4
MCAI s128	spinel	interior	3.7683E-04	1.79E-01	-17.8	2.9	1.9858E-03	8.01E-02	-9.3	3.5	-13.0	2.4 9.8E-04 1.6
MCAI s129	spinel> pervosike	interior	3.6703E-04	1.83E-01	-43.4	2.9	1.9315E-03	7.55E-02	-36.4	3.5	-24.5	2.4 1.2E-06 3.0
MCAI s130	olivine near rim	near edge	3.8092E-04	1.47E-01	-7.2	2.7	1.9927E-03	7.11E-02	-5.8	3.5	-4.1	2.1 1.0E-03 0.8
Secondary												
Sodalite_s119	sodalite near pyroxene		3.8712E-04	1.82E-01	9.0	3.0	2.0378E-03	9.15E-02	16.7	3.5	0.4	2.5 1.9E-03 1.5
Sodalite_s120	sodalite near pyroxene		3.8749E-04	1.85E-01	10.0	3.0	2.0493E-03	8.59E-02	22.4	3.5	-1.6	2.5 1.3E-03 1.5
Standards												
Burma s1	spinel		3.8702E-04	1.54E-01	8.8	1.6	2.0464E-03	8.47E-02	20.9	0.9	-2.1	1.8 4.3E-07 4.5
Burma s2	spinel		3.8840E-04	1.59E-01	12.4	1.6	2.0569E-03	7.48E-02	26.2	0.8	-1.2	1.8 4.7E-07 4.8
Burma s3	spinel		3.8812E-04	1.58E-01	11.6	1.6	2.0491E-03	7.70E-02	22.3	0.8	0.0	1.8 4.1E-07 4.5
Burma s4	spinel		3.8876E-04	1.65E-01	13.3	1.7	2.0493E-03	8.27E-02	22.4	0.8	1.7	1.9 4.1E-07 5.4
Burma s5	spinel		3.8714E-04	1.53E-01	9.1	1.5	2.0445E-03	7.34E-02	20.0	0.7	-1.3	1.7 4.4E-07 4.5
Burma s6	spinel		3.8757E-04	1.68E-01	10.2	1.7	2.0441E-03	8.81E-02	19.8	0.9	-0.1	1.9 4.2E-07 4.9
Burma s7	spinel		3.8892E-04	1.48E-01	13.7	1.5	2.0559E-03	7.05E-02	25.7	0.7	0.4	1.7 3.9E-07 4.7
Burma s8	spinel		3.8775E-04	1.71E-01	10.7	1.7	2.0450E-03	8.54E-02	20.3	0.9	0.1	1.9 4.2E-07 5.0
Burma s9	spinel		3.8718E-04	1.62E-01	9.2	1.6	2.0407E-03	8.43E-02	18.1	0.9	-0.2	1.8 4.3E-07 4.7
Burma s10	spinel		3.9003E-04	1.77E-01	16.6	1.8	2.0606E-03	7.74E-02	28.0	0.8	2.1	2.0 4.2E-07 4.9
Burma s11	spinel		3.8866E-04	1.65E-01	13.1	1.7	2.0564E-03	8.80E-02	25.9	0.9	-0.4	1.9 4.0E-07 5.3
Burma s12	spinel		3.8769E-04	1.53E-01	10.5	1.5	2.0404E-03	7.56E-02	18.0	0.8	1.2	1.7 4.5E-07 5.0
			average	2 SD	average	2 SD	average	2 SD	average	2 SD	average	2 SD
			3.8810E-04	1.78E-06	11.6	4.7	2.0491E-03	1.36E-05	22.3	6.8	0.0	2.5
Burma Spinel True (U Chicago laser assisted flourination, Clayton et al.)												
			3.8753E-04				2.0498E-03					
MiaAn s1	Anorthite		3.8567E-04	1.56E-01	5.2	1.6	2.0240E-03	7.04E-02	9.8	0.7	0.2	1.7
MiaAn s2	Anorthite		3.8539E-04	1.59E-01	4.5	1.6	2.0295E-03	7.15E-02	12.5	0.7	-2.0	1.8
MiaAn s3	Anorthite		3.8352E-04	1.45E-01	-0.4	1.5	2.0022E-03	6.91E-02	-1.1	0.7	0.2	1.6
MiaAn s4	Anorthite		3.8325E-04	1.47E-01	-1.1	1.5	1.9991E-03	7.21E-02	-2.6	0.7	0.3	1.6
MiaAn s5	Anorthite		3.8840E-04	1.50E-01	12.4	1.5	2.0398E-03	7.22E-02	17.7	0.7	3.2	1.7
MiaAn s6	Anorthite		3.8647E-04	1.57E-01	7.3	1.6	2.0274E-03	6.74E-02	11.5	0.7	1.4	1.7
			average	2 SD	average	2 SD	average	2 SD	average	2 SD	average	2 SD
			3.8545E-04	1.92E-06	4.7	10.0	2.0203E-03	1.62E-05	7.9	16.1	0.5	3.4
MiaAn Anorthite (U Hawaii ims 1280 Krot et al.)												
					3.3				6.4		0.0	
SMOW	Reference Value		3.8308E-04		0.0		2.0051E-03		0.0		0.0	
IMF Correction Applied (based on Clayton et al. value versus average measured burma spinel standard value, this study)												
					1.51				-0.37		0.0	

Table S2. Melilite Compositions in Interior of CAI (Traverse 4)

	MEL1	MEL2	MEL3	MEL4	MEL5	MEL6	MEL7	MEL8	MEL9	MEL10
Na ₂ O	0.383	0.009	0.000	0.003	0.000	0.000	0.042	0.046	0.093	0.044
MgO	0.444	1.018	1.348	2.705	3.577	4.045	3.801	3.917	4.128	3.824
Al ₂ O ₃	35.343	34.604	33.482	30.389	27.789	27.041	27.392	26.950	26.627	27.643
SiO ₂	23.134	23.851	24.181	26.213	27.631	28.279	27.845	27.922	28.192	27.903
CaO	40.795	41.330	41.237	41.387	41.474	41.510	41.462	41.481	41.499	41.499
TiO ₂	0.142	0.083	0.105	0.098	0.102	0.100	0.112	0.078	0.132	0.083
FeO	0.181	0.055	0.039	0.027	0.022	0.023	0.024	0.015	0.022	0.000
Sum	100.422	100.950	100.392	100.822	100.595	100.998	100.678	100.409	100.693	100.996
O	7	7	7	7	7	7	7	7	7	7
Na	0.034	0.001	0.000	0.000	0.000	0.000	0.004	0.004	0.008	0.004
Mg	0.030	0.069	0.091	0.182	0.242	0.272	0.257	0.266	0.279	0.257
Al	1.895	1.844	1.794	1.621	1.486	1.439	1.463	1.444	1.423	1.471
Si	1.053	1.078	1.100	1.186	1.253	1.277	1.262	1.270	1.278	1.260
Ca	1.989	2.002	2.009	2.007	2.016	2.008	2.014	2.021	2.016	2.008
Ti	0.005	0.003	0.004	0.003	0.003	0.003	0.004	0.003	0.005	0.003
Fe	0.007	0.002	0.001	0.001	0.001	0.001	0.001	0.001	0.001	0.000
Tot	5.012	4.998	5.000	5.000	5.001	5.000	5.004	5.008	5.010	5.003
Åk(Mg)	3.011	6.860	9.138	18.247	24.187	27.226	25.684	26.552	27.903	25.744
Åk(Al)	5.244	7.824	10.279	18.969	25.725	28.054	26.835	27.787	28.854	26.437
Åk(Si)	5.252	7.813	9.959	18.612	25.326	27.680	26.211	26.962	27.828	26.008
Åk(avg)	4.502	7.499	9.792	18.609	25.079	27.653	26.244	27.100	28.195	26.063
Åk(AlSi)	5.248	7.819	10.119	18.790	25.526	27.867	26.523	27.375	28.341	26.223
Distance from outer edge (µm)	3.1	10.1	13.8	20.3	27.4	29.5	33.9	37.0	39.5	50.7

Table S2. (cont.)

	MEL11	MEL12	MEL10	MEL10B	MEL13	MEL14	MEL15	MEL16	MEL17	MEL18	MEL19	MEL20
Na ₂ O	0.069	0.018	0.040	0.054	0.019	0.023	0.027	0.008	0.024	0.024	0.038	0.022
MgO	4.882	4.799	3.589	4.257	3.894	3.728	4.171	3.983	4.177	4.169	4.603	3.907
Al ₂ O ₃	24.983	24.928	27.645	26.160	27.192	27.322	26.236	27.309	26.285	26.304	24.951	27.039
SiO ₂	29.567	29.512	27.355	28.474	27.999	27.357	28.228	27.933	27.770	27.873	28.793	27.458
CaO	41.401	41.549	41.541	41.443	41.551	41.393	41.423	41.390	41.432	41.295	41.289	41.314
TiO ₂	0.073	0.083	0.092	0.090	0.122	0.122	0.102	0.115	0.138	0.145	0.128	0.122
FeO	0.006	0.005	0.009	0.015	0.022	0.012	0.012	0.012	0.000	0.013	0.006	0.000
Sum	100.981	100.894	100.271	100.493	100.799	99.957	100.199	100.750	99.826	99.823	99.808	99.862
O	7	7	7	7	7	7	7	7	7	7	7	7
Na	0.006	0.002	0.004	0.005	0.002	0.002	0.002	0.001	0.002	0.002	0.003	0.002
Mg	0.328	0.323	0.244	0.288	0.263	0.254	0.283	0.269	0.285	0.284	0.314	0.266
Al	1.329	1.328	1.485	1.400	1.451	1.472	1.409	1.457	1.419	1.419	1.345	1.458
Si	1.334	1.334	1.246	1.293	1.268	1.250	1.286	1.265	1.272	1.276	1.317	1.256
Ca	2.002	2.012	2.028	2.016	2.016	2.027	2.022	2.008	2.033	2.025	2.024	2.025
Ti	0.002	0.003	0.003	0.003	0.004	0.004	0.003	0.004	0.005	0.005	0.004	0.004
Fe	0.000	0.000	0.000	0.001	0.001	0.000	0.000	0.000	0.000	0.000	0.000	0.000
Tot	5.002	5.001	5.010	5.006	5.004	5.010	5.007	5.003	5.015	5.011	5.008	5.012
Åk(Mg)	32.843	32.328	24.379	28.819	26.282	25.404	28.332	26.881	28.516	28.442	31.388	26.645
Åk(Al)	33.564	33.622	25.771	29.995	27.454	26.405	29.555	27.144	29.068	29.064	32.744	27.107
Åk(Si)	33.426	33.356	24.643	29.305	26.762	25.049	28.620	26.459	27.170	27.556	31.706	25.615
Åk(avg)	33.278	33.102	24.931	29.373	26.833	25.619	28.836	26.828	28.251	28.354	31.946	26.456
Åk(AlSi)	33.495	33.489	25.207	29.650	27.108	25.727	29.087	26.802	28.119	28.310	32.225	26.361
Distance from outer edge (µm)	59.0	64.8	54.7	63.6	67.6	71.9	77.2	81.3	85.3	88.2	92.2	95.2

Table S2. (cont.)

	MEL21	MEL23	MEL24	MEL25	MEL26	MEL27	MEL28	MEL29	MEL30
Na ₂ O	0.018	0.019	0.004	0.000	0.003	0.003	0.004	0.005	0.007
MgO	4.360	4.904	4.598	4.038	4.390	4.443	4.149	4.247	4.247
Al ₂ O ₃	25.323	24.427	24.987	26.449	25.863	25.811	26.175	26.362	26.445
SiO ₂	28.142	28.145	28.059	26.716	27.265	27.770	28.008	27.999	27.719
CaO	41.237	41.053	41.008	41.181	41.079	41.303	41.373	41.521	41.342
TiO ₂	0.108	0.060	0.090	0.145	0.153	0.142	0.155	0.162	0.163
FeO	0.005	0.003	0.008	0.008	0.000	0.004	0.010	0.005	0.001
Sum	99.193	98.611	98.754	98.537	98.753	99.476	99.874	100.301	99.924
O	7	7	7	7	7	7	7	7	7
Na	0.002	0.002	0.000	0.000	0.000	0.000	0.000	0.000	0.001
Mg	0.299	0.339	0.317	0.280	0.303	0.304	0.283	0.288	0.290
Al	1.375	1.336	1.363	1.449	1.413	1.398	1.411	1.415	1.425
Si	1.297	1.306	1.299	1.242	1.264	1.277	1.281	1.275	1.268
Ca	2.036	2.041	2.034	2.051	2.040	2.034	2.027	2.026	2.026
Ti	0.004	0.002	0.003	0.005	0.005	0.005	0.005	0.006	0.006
Fe	0.000	0.000	0.000	0.000	0.000	0.000	0.000	0.000	0.000
Tot	5.013	5.025	5.017	5.028	5.025	5.019	5.008	5.012	5.014
Åk(Mg)	29.949	33.917	31.728	27.988	30.330	30.449	28.289	28.840	28.954
Åk(Al)	31.241	33.218	31.845	27.535	29.368	30.077	29.453	29.238	28.734
Åk(Si)	29.671	30.576	29.877	24.213	26.357	27.663	28.100	27.538	26.762
Åk(avg)	30.287	32.570	31.150	26.578	28.685	29.396	28.614	28.538	28.150
Åk(AlSi)	30.456	31.897	30.861	25.874	27.863	28.870	28.776	28.388	27.748
Distance from outer edge (µm)	99.7	101.3	103.4	112.1	115.6	125.2	130.9	137.1	140.6

Table S2. (cont.)

	MEL31	MEL32	MEL33	MEL34	MEL35	MEL36	MEL37	MEL40
Na ₂ O	0.008	0.001	0.000	0.000	0.013	0.049	0.009	0.005
MgO	4.191	4.073	4.036	3.953	4.970	4.756	5.366	4.375
Al ₂ O ₃	26.071	26.360	27.239	26.444	24.558	25.238	23.725	25.941
SiO ₂	27.775	27.772	27.700	27.518	29.418	28.771	29.681	28.087
CaO	41.517	41.377	41.442	40.978	41.530	40.908	41.349	41.271
TiO ₂	0.163	0.158	0.143	0.147	0.113	0.225	0.304	0.162
FeO	0.000	0.001	0.013	0.004	0.001	0.059	0.033	0.008
Sum	99.725	99.742	100.573	99.044	100.603	100.006	100.467	99.849
O	7	7	7	7	7	7	7	7
Na	0.001	0.000	0.000	0.000	0.001	0.004	0.001	0.000
Mg	0.287	0.278	0.273	0.272	0.336	0.323	0.363	0.298
Al	1.409	1.423	1.457	1.437	1.313	1.356	1.270	1.398
Si	1.274	1.272	1.257	1.269	1.334	1.312	1.348	1.285
Ca	2.040	2.031	2.016	2.025	2.018	1.999	2.012	2.023
Ti	0.006	0.005	0.005	0.005	0.004	0.008	0.010	0.006
Fe	0.000	0.000	0.000	0.000	0.000	0.002	0.001	0.000
Tot	5.016	5.011	5.009	5.007	5.006	5.004	5.007	5.011
Åk(Mg)	28.655	27.818	27.313	27.173	33.603	32.329	36.337	29.834
Åk(Al)	29.537	28.834	27.133	28.145	34.365	32.185	36.493	30.075
Åk(Si)	27.388	27.236	25.745	26.887	33.423	31.190	34.825	28.476
Åk(avg)	28.527	27.963	26.731	27.402	33.797	31.901	35.885	29.462
Åk(AlSi)	28.463	28.035	26.439	27.516	33.894	31.687	35.659	29.276
Distance from outer edge (µm)	145.1	149.2	153.4	159.1	162.5	167.6	171.0	177.5

Table S2. (cont.)

	MEL41	MEL42	MEL43	MEL44	MEL45	MEL46
Na ₂ O	0.001	0.015	0.001	0.008	0.000	0.001
MgO	4.713	5.321	4.416	4.174	4.323	4.469
Al ₂ O ₃	25.059	23.498	25.557	26.351	26.504	25.520
SiO ₂	28.778	29.621	28.230	28.014	27.909	28.620
CaO	41.577	41.563	41.594	41.464	41.358	41.489
TiO ₂	0.115	0.118	0.123	0.112	0.105	0.053
FeO	0.012	0.010	0.019	0.018	0.001	0.010
Sum	100.255	100.146	99.940	100.141	100.200	100.162
O	7	7	7	7	7	7
Na	0.000	0.001	0.000	0.001	0.000	0.000
Mg	0.320	0.362	0.301	0.284	0.294	0.304
Al	1.346	1.263	1.378	1.417	1.424	1.371
Si	1.311	1.351	1.292	1.278	1.272	1.305
Ca	2.030	2.031	2.039	2.027	2.020	2.026
Ti	0.004	0.004	0.004	0.004	0.004	0.002
Fe	0.000	0.000	0.001	0.001	0.000	0.000
Tot	5.012	5.014	5.015	5.010	5.013	5.008
Åk(Mg)	32.016	36.186	30.121	28.385	29.372	30.369
Åk(Al)	32.709	36.833	31.093	29.166	28.818	31.447
Åk(Si)	31.137	35.125	29.163	27.790	27.198	30.463
Åk(avg)	31.954	36.048	30.126	28.447	28.462	30.760
Åk(AlSi)	31.923	35.979	30.128	28.478	28.008	30.955
Distance from outer edge (µm)	182.0	185.1	189.3	191.3	196.2	199.9

Table S3. Representative Compositions of Minerals of Wark-Lovering Rim

	Hibonite	Hibonite	Hibonite	Spinel	Spinel	Spinel	Pyroxene	Pyroxene	Pyroxene	Olivine	Olivine	Olivine
	RIMHIB2	R4 HIB1	RIMHIB3	RIMSP3	RIMSP2	R2 SP2	R2 PYX2	R2 PYX1	PYX2	OL4	R30L2	R20L1
MgO	1.92	2.69	3.40	22.00	24.33	25.32	18.68	15.09	14.67	50.19	43.09	39.21
Al ₂ O ₃	86.74	84.07	82.54	67.82	69.15	69.46	1.38	7.57	8.86	0.00	0.01	0.13
SiO ₂	0.27	0.15	0.08	0.04	0.02	0.03	54.14	50.28	48.69	40.89	38.95	37.95
CaO	8.32	8.32	8.31	0.10	0.11	0.09	23.89	24.77	25.52	0.08	0.12	0.16
TiO ₂	3.14	4.87	5.93	0.22	0.23	0.14	0.10	0.53	1.93	0.02	0.02	0.01
Cr ₂ O ₃	n.a.	n.a.	n.a.	0.11	0.10	0.14	0.07	0.10	0.09	0.02	0.00	0.15
MnO	n.a.	n.a.	n.a.	0.03	0.03	0.03	0.00	0.06	0.06	0.09	0.12	0.15
FeO	0.20	0.22	0.21	10.30	7.04	5.87	1.34	1.53	0.28	10.28	19.38	23.47
Sum	100.59	100.33	100.47	100.62	101.01	101.07	99.60	99.93	100.08	101.56	101.69	101.23
Mg	0.318	0.449	0.570	0.809	0.879	0.909	1.009	0.817	0.793	1.809	1.620	1.511
Al	11.387	11.115	10.928	1.974	1.975	1.973	0.059	0.324	0.378	0.000	0.000	0.004
Si	0.030	0.017	0.009	0.001	0.001	0.001	1.963	1.826	1.765	0.989	0.982	0.981
Ca	0.993	1.001	1.000	0.003	0.003	0.002	0.928	0.964	0.991	0.002	0.003	0.004
Ti	0.263	0.411	0.501	0.004	0.004	0.003	0.003	0.014	0.053	0.000	0.000	0.000
Cr	n.a.	n.a.	n.a.	0.002	0.002	0.003	0.002	0.003	0.002	0.000	0.000	0.003
Mn	n.a.	n.a.	n.a.	0.001	0.001	0.001	0.000	0.002	0.002	0.002	0.003	0.003
Fe	0.019	0.021	0.020	0.213	0.143	0.118	0.041	0.047	0.008	0.208	0.409	0.508
Total cations	13.015	13.015	13.027	3.007	3.007	3.010	4.004	3.996	3.992	3.011	3.017	3.015
Number of O atoms	19	19	19	4	4	4	6	6	6	4	4	4

n.a.: not analyzed